University Library



A gateway to Melbourne's research publications

Minerva Access is the Institutional Repository of The University of Melbourne

Author/s:
Omori, Y;Giannantonio, T;Porredon, A;Baxter, EJ;Chang, C;Crocce, M;Fosalba, P;Alarcon, A;Banik, N;Blazek, J;Bleem, LE;Bridle, SL;Cawthon, R;Choi, A;Chown, R;Crawford, T;Dodelson, S;Drlica-Wagner, A;Eifler, TF;Elvin-Poole, J;Friedrich, O;Gruen, D;Holder, GP;Huterer, D;Jain, B;Jarvis, M;Kirk, D;Kokron, N;Krause, E;Maccrann, N;Muir, J;Prat, J;Reichardt, CL;Ross, AJ;Rozo, E;Rykoff, ES;Sánchez, C;Secco, LF;Simard, G;Wechsler, RH;Zuntz, J;Abbott, TMC;Abdalla, FB;Allam, S;Avila, S;Aylor, K;Benson, BA;Bernstein, GM;Bertin, E;Bianchini, F;Brooks, D;Buckley-Geer, E;Burke, DL;Carlstrom, JE;Carnero Rosell, A;Carrasco Kind, M;Carretero, J;Castander, FJ;Chang, CL;Cho, HM;Crites, AT;Cunha, CE;Da Costa, LN;De Haan, T;Davis, C;De Vicente, J;Desai, S;Diehl, HT;Dietrich, JP;Dobbs, MA;Everett, WB;Doel, P;Estrada, J;Flaugher, B;Frieman, J;García-Bellido, J;Gaztanaga, E;Gerdes, DW;George, EM;Gruendl, RA;Gschwend, J;Gutierrez, G;Halverson, NW;Harrington, NL;Hartley, WG;Hollowood, DL;Holzapfel, WL;Honscheid, K;Hou, Z;Hoyle, B;Hrubes, JD;James, DJ;Jeltema, T;Kuehn, K;Kuropatkin, N;Lee, AT;Leitch, EM;Lima, M;Luong-Van, D

Title:
Dark Energy Survey Year 1 Results: Tomographic cross-correlations between Dark Energy Survey galaxies and CMB lensing from South Pole Telescope+Planck

Date:
2019-08-01

Citation:
Omori, Y., Giannantonio, T., Porredon, A., Baxter, E. J., Chang, C., Crocce, M., Fosalba, P., Alarcon, A., Banik, N., Blazek, J., Bleem, L. E., Bridle, S. L., Cawthon, R., Choi, A., Chown, R., Crawford, T., Dodelson, S., Drlica-Wagner, A., Eifler, T. F. ,... Luong-Van, D. (2019). Dark Energy Survey Year 1 Results: Tomographic cross-correlations between Dark Energy Survey galaxies and CMB lensing from South Pole Telescope+Planck. Physical Review D, 100 (4), https://doi.org/10.1103/PhysRevD.100.043501.

Persistent Link:
https://hdl.handle.net/11343/227692

Dark Energy Survey Year 1 Results: Tomographic cross-correlations between Dark Energy Survey galaxies and CMB lensing from South Pole Telescope + Planck

Y. Omori,[1,2,3] T. Giannantonio,[4,5,6] A. Porredon,[7,8] E. J. Baxter,[9] C. Chang,[10] M. Crocce,[7,8] P. Fosalba,[7,8] A. Alarcon,[7,8] N. Banik,[11] J. Blazek,[12,13] L. E. Bleem,[10,14] S. L. Bridle,[15] R. Cawthon,[10] A. Choi,[12] R. Chown,[16,3] T. Crawford,[17,10] S. Dodelson,[18] A. Drlica-Wagner,[11] T. F. Eifler,[19,20] J. Elvin-Poole,[15] O. Friedrich,[21,6] D. Gruen,[2,22] G. P. Holder,[3,23–25] D. Huterer,[26] B. Jain,[9] M. Jarvis,[9] D. Kirk,[27] N. Kokron,[1,2] E. Krause,[19] N. MacCrann,[12,28] J. Muir,[2] J. Prat,[29] C. L. Reichardt,[30] A. J. Ross,[12] E. Rozo,[31] E. S. Rykoff,[2,22] C. Sánchez,[9,29] L. F. Secco,[9] G. Simard,[3] R. H. Wechsler,[1,2,22] J. Zuntz,[32] T. M. C. Abbott,[33] F. B. Abdalla,[27,34] S. Allam,[11] S. Avila,[35] K. Aylor,[36] B. A. Benson,[10,11,17] G. M. Bernstein,[9] E. Bertin,[37,38] F. Bianchini,[30] D. Brooks,[27] E. Buckley-Geer,[11] D. L. Burke,[2,22] J. E. Carlstrom,[10,17,14,39,40] A. Carnero Rosell,[41,42] M. Carrasco Kind,[24,43] J. Carretero,[29] F. J. Castander,[7,8] C. L. Chang,[10,17,14] H-M. Cho,[22] A. T. Crites,[44] C. E. Cunha,[2] L. N. da Costa,[42] T. de Haan,[45,46] C. Davis,[2] J. De Vicente,[47] S. Desai,[48] H. T. Diehl,[11] J. P. Dietrich,[49,50] M. A. Dobbs,[3,51] W. B. Everett,[52] P. Doel,[27] J. Estrada,[11] B. Flaugher,[11] J. Frieman,[10,11] J. García-Bellido,[53] E. Gaztanaga,[7,8] D. W. Gerdes,[26,54] E. M. George,[45,55] R. A. Gruendl,[24,43] J. Gschwend,[41,42] G. Gutierrez,[11] N. W. Halverson,[52,56] N. L. Harrington,[45] W. G. Hartley,[27,57] D. L. Hollowood,[58] W. L. Holzapfel,[45] K. Honscheid,[12,28] Z. Hou,[10,17] B. Hoyle,[21,6] J. D. Hrubes,[59] D. J. James,[60] T. Jeltema,[58] K. Kuehn,[61] N. Kuropatkin,[11] A. T. Lee,[45,46] E. M. Leitch,[10,17] M. Lima,[62,41] D. Luong-Van,[59] A. Manzotti,[63,10,17] D. P. Marrone,[64] J. L. Marshall,[65] J. J. McMahon,[26] P. Melchior,[66] F. Menanteau,[24,43] S. S. Meyer,[10,17,40,67] C. J. Miller,[26,54] R. Miquel,[29,68] L. M. Mocanu,[10,17] J. J. Mohr,[21,49,50] T. Natoli,[10,39,69] S. Padin,[10,17] A. A. Plazas,[20] C. Pryke,[70] A. K. Romer,[71] A. Roodman,[2,22] J. E. Ruhl,[72] E. Sanchez,[47] V. Scarpine,[11] K. K. Schaffer,[10,40,73] M. Schubnell,[26] S. Serrano,[7,8] I. Sevilla-Noarbe,[47] E. Shirokoff,[10,17,45] M. Smith,[74] M. Soares-Santos,[75] F. Sobreira,[41,76] Z. Staniszewski,[72,20] A. A. Stark,[60] K. T. Story,[2,1] E. Suchyta,[77] M. E. C. Swanson,[43] G. Tarle,[26] D. Thomas,[35] M. A. Troxel,[12,28] K. Vanderlinde,[69,78] J. D. Vieira,[24,25] A. R. Walker,[33] W. L. K. Wu,[10] and O. Zahn[79]

(DES and SPT Collaborations)

[1]*Department of Physics, Stanford University, 382 Via Pueblo Mall, Stanford, California 94305, USA*
[2]*Kavli Institute for Particle Astrophysics and Cosmology, P.O. Box 2450, Stanford University, Stanford, California 94305, USA*
[3]*Department of Physics and McGill Space Institute, McGill University, Montreal, Quebec H3A 2T8, Canada*
[4]*Institute of Astronomy, University of Cambridge, Madingley Road, Cambridge CB3 0HA, United Kingdom*
[5]*Kavli Institute for Cosmology, University of Cambridge, Madingley Road, Cambridge CB3 0HA, United Kingdom*
[6]*Universitäts-Sternwarte, Fakultät für Physik, Ludwig-Maximilians Universität München, Scheinerstrasse 1, 81679 München, Germany*
[7]*Institut d'Estudis Espacials de Catalunya (IEEC), 08193 Barcelona, Spain*
[8]*Institute of Space Sciences (ICE, CSIC), Campus UAB, Carrer de Can Magrans, s/n, 08193 Barcelona, Spain*
[9]*Department of Physics and Astronomy, University of Pennsylvania, Philadelphia, Pennsylvania 19104, USA*
[10]*Kavli Institute for Cosmological Physics, University of Chicago, Chicago, Illinois 60637, USA*
[11]*Fermi National Accelerator Laboratory, P.O. Box 500, Batavia, Illinois 60510, USA*
[12]*Center for Cosmology and Astro-Particle Physics, The Ohio State University, Columbus, Ohio 43210, USA*
[13]*Institute of Physics, Laboratory of Astrophysics, École Polytechnique Fédérale de Lausanne (EPFL), Observatoire de Sauverny, 1290 Versoix, Switzerland*
[14]*High Energy Physics Division, Argonne National Laboratory, Argonne, Illinois 60439, USA*
[15]*Jodrell Bank Center for Astrophysics, School of Physics and Astronomy, University of Manchester, Oxford Road, Manchester, M13 9PL, United Kingdom*
[16]*Department of Physics and Astronomy, McMaster University, 1280 Main Street West, Hamilton, Ontario L8S 4L8, Canada*
[17]*Department of Astronomy and Astrophysics, University of Chicago, Chicago, Illinois 60637, USA*

 © 2019 American Physical Society

[18]*Department of Physics, Carnegie Mellon University, Pittsburgh, Pennsylvania 15312, USA*
[19]*Department of Astronomy/Steward Observatory, 933 North Cherry Avenue, Tucson, Arizona 85721-0065, USA*
[20]*Jet Propulsion Laboratory, California Institute of Technology, 4800 Oak Grove Drive, Pasadena, California 91109, USA*
[21]*Max Planck Institute for Extraterrestrial Physics, Giessenbachstrasse, 85748 Garching, Germany*
[22]*SLAC National Accelerator Laboratory, Menlo Park, California 94025, USA*
[23]*Canadian Institute for Advanced Research, CIFAR Program in Cosmology and Gravity, Toronto, Ontario, M5G 1Z8, Canada*
[24]*Department of Astronomy, University of Illinois at Urbana-Champaign, 1002 West Green Street, Urbana, Illinois 61801, USA*
[25]*Department of Physics, University of Illinois Urbana-Champaign, 1110 West Green Street, Urbana, Illinois 61801, USA*
[26]*Department of Physics, University of Michigan, Ann Arbor, Michigan 48109, USA*
[27]*Department of Physics and Astronomy, University College London, Gower Street, London, WC1E 6BT, United Kingdom*
[28]*Department of Physics, The Ohio State University, Columbus, Ohio 43210, USA*
[29]*Institut de Física d'Altes Energies (IFAE), The Barcelona Institute of Science and Technology, Campus UAB, 08193 Bellaterra (Barcelona), Spain*
[30]*School of Physics, University of Melbourne, Parkville, Victoria 3010, Australia*
[31]*Department of Physics, University of Arizona, Tucson, Arizona 85721, USA*
[32]*Institute for Astronomy, University of Edinburgh, Edinburgh EH9 3HJ, United Kingdom*
[33]*Cerro Tololo Inter-American Observatory, National Optical Astronomy Observatory, Casilla 603, La Serena, Chile*
[34]*Department of Physics and Electronics, Rhodes University, P.O. Box 94, Grahamstown, 6140, South Africa*
[35]*Institute of Cosmology and Gravitation, University of Portsmouth, Portsmouth, PO1 3FX, United Kingdom*
[36]*Department of Physics, University of California, Davis, California 95616, USA*
[37]*CNRS, UMR 7095, Institut d'Astrophysique de Paris, F-75014, Paris, France*
[38]*Sorbonne Universités, UPMC Université Paris 06, UMR 7095, Institut d'Astrophysique de Paris, F-75014, Paris, France*
[39]*Department of Physics, University of Chicago, Chicago, Illinois 60637, USA*
[40]*Enrico Fermi Institute, University of Chicago, Chicago, Illinois 60637, USA*
[41]*Laboratório Interinstitucional de e-Astronomia—LIneA, Rua Gal. José Cristino 77, Rio de Janeiro, RJ—20921-400, Brazil*
[42]*Observatório Nacional, Rua Gal. José Cristino 77, Rio de Janeiro, RJ—20921-400, Brazil*
[43]*National Center for Supercomputing Applications, 1205 West Clark Street, Urbana, Illinois 61801, USA*
[44]*California Institute of Technology, Pasadena, California 91125, USA*
[45]*Department of Physics, University of California, Berkeley, California 94720, USA*
[46]*Physics Division, Lawrence Berkeley National Laboratory, Berkeley, California 94720, USA*
[47]*Centro de Investigaciones Energéticas, Medioambientales y Tecnológicas (CIEMAT), Madrid, Spain*
[48]*Department of Physics, IIT Hyderabad, Kandi, Telangana 502285, India*
[49]*Excellence Cluster Universe, Boltzmannstrasse 2, 85748 Garching, Germany*
[50]*Faculty of Physics, Ludwig-Maximilians-Universität, Scheinerstrasse 1, 81679 Munich, Germany*
[51]*Canadian Institute for Advanced Research, CIFAR Program in Gravity and the Extreme Universe, Toronto, Ontario, M5G 1Z8, Canada*
[52]*Center for Astrophysics and Space Astronomy, Department of Astrophysical and Planetary Sciences, University of Colorado, Boulder, Colorado 80309, USA*
[53]*Instituto de Fisica Teorica UAM/CSIC, Universidad Autonoma de Madrid, 28049 Madrid, Spain*
[54]*Department of Astronomy, University of Michigan, Ann Arbor, Michigan 48109, USA*
[55]*European Southern Observatory, Karl-Schwarzschild-Straße 2, 85748 Garching, Germany*
[56]*Department of Physics, University of Colorado, Boulder, Colorado 80309, USA*
[57]*Department of Physics, ETH Zurich, Wolfgang-Pauli-Strasse 16, CH-8093 Zurich, Switzerland*
[58]*Santa Cruz Institute for Particle Physics, Santa Cruz, California 95064, USA*
[59]*University of Chicago, Chicago, Illinois 60637, USA*
[60]*Harvard-Smithsonian Center for Astrophysics, Cambridge, Massachusetts 02138, USA*
[61]*Australian Astronomical Observatory, North Ryde, New South Wales 2113, Australia*
[62]*Departamento de Física Matemática, Instituto de Física, Universidade de São Paulo, C.P. 66318, São Paulo, SP, 05314-970, Brazil*

[63]Institut d'Astrophysique de Paris, F-75014, Paris, France
[64]Steward Observatory, University of Arizona, 933 North Cherry Avenue, Tucson, Arizona 85721, USA
[65]George P. and Cynthia Woods Mitchell Institute for Fundamental Physics and Astronomy, and Department of Physics and Astronomy, Texas A&M University, College Station, Texas 77843, USA
[66]Department of Astrophysical Sciences, Princeton University, Peyton Hall, Princeton, New Jersey 08544, USA
[67]Department of Physics, University of Chicago, Chicago, Illinois 6063, USA
[68]Institució Catalana de Recerca i Estudis Avançats, E-08010 Barcelona, Spain
[69]Dunlap Institute for Astronomy and Astrophysics, University of Toronto, 50 St. George Street, Toronto, Ontario, M5S 3H4, Canada
[70]Department of Physics, University of Minnesota, Minneapolis, Minnesota 55455, USA
[71]Department of Physics and Astronomy, Pevensey Building, University of Sussex, Brighton, BN1 9QH, United Kingdom
[72]Physics Department, Center for Education and Research in Cosmology and Astrophysics, Case Western Reserve University, Cleveland, Ohio 44106, USA
[73]Liberal Arts Department, School of the Art Institute of Chicago, Chicago, Illinois 60603, USA
[74]School of Physics and Astronomy, University of Southampton, Southampton, SO17 1BJ, United Kingdom
[75]Brandeis University, Physics Department, 415 South Street, Waltham, Massachusetts 02453, USA
[76]Instituto de Física Gleb Wataghin, Universidade Estadual de Campinas, 13083-859, Campinas, SP, Brazil
[77]Computer Science and Mathematics Division, Oak Ridge National Laboratory, Oak Ridge, Tennessee 37831, USA
[78]Department of Astronomy and Astrophysics, University of Toronto, 50 St. George Street, Toronto, Ontario, M5S 3H4, Canada
[79]Berkeley Center for Cosmological Physics, Department of Physics, University of California, and Lawrence Berkeley National Labs, Berkeley, California 94720, USA

(Received 2 November 2018; published 1 August 2019)

We measure the cross-correlation between REDMAGIC galaxies selected from the Dark Energy Survey (DES) year 1 data and gravitational lensing of the cosmic microwave background (CMB) reconstructed from South Pole Telescope (SPT) and *Planck* data over 1289 deg^2. When combining measurements across multiple galaxy redshift bins spanning the redshift range of $0.15 < z < 0.90$, we reject the hypothesis of no correlation at 19.9σ significance. When removing small-scale data points where thermal Sunyaev-Zel'dovich signal and nonlinear galaxy bias could potentially bias our results, the detection significance is reduced to 9.9σ. We perform a joint analysis of galaxy-CMB lensing cross-correlations and galaxy clustering to constrain cosmology, finding $\Omega_{\rm m} = 0.276^{+0.029}_{-0.030}$ and $S_8 = \sigma_8\sqrt{\Omega_{\rm m}/0.3} = 0.800^{+0.090}_{-0.094}$. We also perform two alternate analyses aimed at constraining only the growth rate of cosmic structure as a function of redshift, finding consistency with predictions from the concordance ΛCDM model. The measurements presented here are part of a joint cosmological analysis that combines galaxy clustering, galaxy lensing and CMB lensing using data from DES, SPT and *Planck*.

DOI: 10.1103/PhysRevD.100.043501

I. INTRODUCTION

The cosmic microwave background (CMB) is one of the fundamental cosmological observables. Measurements of primary anisotropies in the CMB, sourced by fluctuations in the photon-baryon fluid at the time of recombination, have been used to place tight constraints on the physical properties of the Universe, most recently by the *Planck* satellite mission [1].

In addition to the information contained in the primary CMB anisotropy, there is also a wealth of information in secondary anisotropies resulting from perturbations to CMB light after the time of recombination [2]. A particularly interesting source of secondary anisotropy is gravitational lensing, which causes the paths of photons from the last-scattering surface to be perturbed by the matter in the Universe (see the review by [3]). These deflections, on the order of a few arcminutes [4], alter the CMB primary anisotropies by redistributing power across different angular scales and producing a non-Gaussian component to the primordial distribution of temperature anisotropies. Measurement of this non-Gaussian structure can be used to infer the total amount of deflection that has occurred in a given direction [5,6]. High signal-to-noise measurements of CMB lensing have been obtained by several collaborations, including the Atacama Cosmology Telescope [7,8], *Planck* [9–11],

POLARBEAR [12], and the South Pole Telescope (SPT) [13–15].

The reconstructed CMB lensing signal is an integral of all deflections sourced by the large-scale structure between the last-scattering surface and us. Due to this projection, we cannot directly measure the evolution of structure along the line of sight by analyzing the lensing signal alone. However, the signal from CMB lensing can be *cross-correlated* with tracers of the matter distribution, such as galaxy catalogs with known redshifts. This allows us to measure the growth of structure in the Universe across cosmic time.

Galaxy density-CMB lensing cross-correlations have been detected by several groups, using a variety of datasets. The first significant detection was reported by [16] correlating WMAP data with radio galaxies from NRAO VLA Sky Survey [17], which was later combined with other galaxy catalogs by [18]. Other recent galaxy-CMB lensing cross-correlation measurements include the cross-correlation with quasars [19–22], with optical, IR and radio galaxies [23–32], the cosmic infrared background [33–36], galaxy clusters [37,38], and many others. The first *tomographic* cross-correlation analysis using multiple redshift bins from a single galaxy survey was carried out by [39] (hereafter G16) using CMB lensing data from SPT and *Planck* and the Dark Energy Survey (DES) Science Verification (SV) galaxies.

In this work, we update the results of G16 by measuring the cross-correlations between galaxy density from the DES Year 1 (Y1) data and a CMB lensing reconstruction using a combination of SPT and *Planck* data in the SPT-SZ survey area.[1] The total area used in this work is nearly a factor of 10 larger than in G16. We find a highly significant detection of the correlation between galaxy density and CMB lensing. We subject the correlation function measurements and corresponding covariance estimates to several tests for systematic effects, finding that biases due to these systematic effects are negligible over the range of angular scales used for the main analysis.

We use the measured galaxy-CMB lensing cross-correlations to extract cosmological information in several ways. First, assuming a fiducial cosmological model based on the results of [41], we measure the amplitude of our measurement relative to this model. The amplitude we obtain from this procedure can be directly compared with similar constraints obtained in previous studies. Second, we infer the linear growth function over the redshift ranges that DES is sensitive to and compare that with the baseline ΛCDM model predictions derived from CMB observations. Two different approaches are used: (i) the $D_{\rm G}$ estimator introduced in G16 and (ii) a method that allows us to marginalize over galaxy bias parameters and parameters associated with systematic measurement errors. Finally, we fix the lensing amplitude and growth-rate parameters to their ΛCDM values and simultaneously estimate cosmological and systematics parameters.

In some of these analyses, we perform joint fits to both the galaxy-CMB lensing cross-correlations and galaxy clustering measurements in order to break degeneracies with galaxy bias.

The measurements presented in this study are part of the joint analysis which also involves galaxy clustering, galaxy-galaxy lensing and cosmic shear measurements presented in [42] and also galaxy weak lensing-CMB weak lensing correlation presented in [43]. The methods that will be used to combine these datasets are described in [44], and the results are presented in [45].

This paper is structured as follows. We first review in Sec. II the theoretical foundations of CMB lensing and galaxy clustering; we then describe the DES, SPT and *Planck* data we use in Sec. III, and the analysis methods we follow in Sec. IV. The tests for possible systematics are described in Sec. V, and the main results of this paper, together with their cosmological implications, are presented in Sec. VI. We finally conclude in Sec. VII.

II. THEORY

From the CMB lensing convergence $\kappa_{\rm CMB}$ and galaxy overdensity $\delta_{\rm g}$ fields, one can construct the auto- and cross-angular power spectra, which can be written as a function of multipole ℓ using the Limber approximation[2] as

$$C^{\delta_{\rm g}^i\delta_{\rm g}^i}(\ell)=\int d\chi\frac{q_{\delta_{\rm g}^i}(\frac{\ell+\frac{1}{2}}{\chi},\chi)q_{\delta_{\rm g}^i}(\frac{\ell+\frac{1}{2}}{\chi},\chi)}{\chi^2}P_{\rm NL}\left(\frac{\ell+\frac{1}{2}}{\chi},z(\chi)\right), \tag{1}$$

$$C^{\delta_{\rm g}^i\kappa_{\rm CMB}}(\ell)=\int d\chi\frac{q_{\delta_{\rm g}^i}(\frac{\ell+\frac{1}{2}}{\chi},\chi)q_{\kappa_{\rm CMB}}(\chi)}{\chi^2}P_{\rm NL}\left(\frac{\ell+\frac{1}{2}}{\chi},z(\chi)\right), \tag{2}$$

where χ is the comoving distance to redshift z, $P_{\rm NL}(k,z)$ is the nonlinear matter power spectrum, and the galaxy and CMB lensing kernels are, respectively,

$$q_{\delta_{\rm g}^i}(k,\chi)=b_{\rm g}^i(k,z(\chi))\frac{n_{\rm g}^i(z(\chi))}{\bar{n}_{\rm g}^i}\frac{dz}{d\chi}, \tag{3}$$

$$q_{\kappa_{\rm CMB}}(\chi)=\frac{3H_0^2\Omega_{\rm m}}{2c^2}\frac{\chi}{a(\chi)}\frac{\chi^*-\chi}{\chi^*}. \tag{4}$$

[1]G16 cross-correlated galaxies with CMB lensing maps from SPT and *Planck* separately, whereas in this study, a lensing map derived from a combined temperature map presented in [40] is used.

[2]See [46] for a discussion regarding the validity of the Limber approximation in the DES multiprobe framework.

Here $b_g^i(k,z)$ is the galaxy bias, $n_g^i(z)$ is the redshift distribution of the ith galaxy sample with total density $\bar{n}_g^i$, a is the cosmological scale factor, and χ^* is the comoving distance to the horizon. We adopt a linear galaxy bias model (i.e., constant value for all values of k) with a single galaxy bias b^i parameter for each galaxy redshift bin. Following [44,46], we restrict the analysis to angular scales over which the linear bias approximation is accurate.

In order to be consistent with the filtering that has been applied to the CMB lensing maps (see Sec. III B), we multiply $C^{\delta_g\kappa_{\rm CMB}}(\ell)$ by the filter function $F(\ell)$, given by

$$F(\ell)=\begin{cases}\exp(-\ell(\ell+1)/\ell_{\rm beam}^2), & \text{for } 30<\ell<3000,\\ 0, & \text{otherwise,}\end{cases} \quad (5)$$

where $\ell_{\rm beam}\equiv\sqrt{16\ln 2}/\theta_{\rm FWHM}$ and $\theta_{\rm FWHM}=5.4'$. The Gaussian filtering is equivalent to convolving the CMB lensing maps with a Gaussian beam of full width at half maximum $\theta_{\rm FWHM}$.

The harmonic-space expression above can be rewritten in position space by applying a Legendre transformation, yielding the two-point correlation functions between two fields a and b:

$$w^{ab}(\theta)=\sum_{\ell=0}^{\infty}\left(\frac{2\ell+1}{4\pi}\right)P_\ell(\cos\theta)C^{ab}(\ell)F(\ell), \quad (6)$$

where $a,b\in\{\delta_g^i,\kappa_{\rm CMB}\}$, P_ℓ are the Legendre polynomials, and the summation can be truncated to $\ell_{\rm max}\sim 10^4$ for the angular scales of interest.

Following [44,46], we model potential biases in the estimation of the galaxy redshift distributions using a single additive bias parameter for each galaxy redshift bin. The galaxy $n(z)$ is modified via

$$n^i_{\rm g,unbiased}(z)=n_g^i(z-\Delta^i_{z,g}), \quad (7)$$

where $\Delta^i_{z,g}$ is the bias parameter. The biased $n_g^i(z)$ is then propagated to the $C^{\delta_g\kappa_{\rm CMB}}(\ell)$ as described above.

We calculate the power spectrum using the Boltzmann code CAMB[3] [48,49] with the Halofit extension to nonlinear scales [50,51] and the [52] neutrino extension.

III. DATA

A. Galaxy samples

Our analysis relies on data from first-year DES observations, which were taken between August 2013 and February 2014. The photometry and production of the science-grade "gold" catalog are described in [53]. The total footprint of Y1 observations with an exposure time >90 s per filter and a valid photometric calibration covers more than 1800 deg^2, which is reduced to $\sim$1500 deg^2 after masking for bright stars and other poor-quality regions, including the Large Magellanic Cloud.

TABLE I. Summary statistics of the DES red-sequence galaxy samples (REDMAGIC) used throughout this paper. The effective sky area covered by these samples is 1289 deg^2.

Luminosity	Redshift range	$\bar{n}_g^i$
$L>0.5L_*$	0.15–0.30	61 913
	0.30–0.45	158 616
	0.45–0.60	234 204
$L>1.0L_*$	0.60–0.75	139 707
$L>1.5L_*$	0.75–0.90	41 270
Total	0.15–0.90	635 710

For the galaxy sample in this work, we use the lens galaxy catalog from [42]. The large-scale clustering properties of these galaxies are described in detail in [54]. This galaxy catalog was generated using the REDMAGIC algorithm [55], which is designed to find red-sequence galaxies in photometric data. The resulting galaxy sample has a photometric redshift uncertainty of $\sigma_z/(1+z)\leq 2\%$, over the entire redshift range $0.15<z<0.90$ used in this analysis. We split this into five tomographic bins of width $\Delta z=0.15$, as shown in Table I.

REDMAGIC produces luminosity-thresholded samples of constant comoving densities to avoid density variations that may lead to biases in clustering analyses. Therefore, setting the luminosity threshold high leads to a sample with lower overall output number density. Following [54], we use three different luminosity cuts ($L>0.5L_*$, $L>1.0L_*$, and $L>1.5L_*$); using a lower luminosity threshold for the three low redshift bins allows for a higher number density in these redshift bins while the two higher redshift bins require a higher luminosity cut to produce a sample with uniform density across the footprint.

We estimate the redshift distributions of our galaxy samples by assuming a Gaussian redshift probability distribution function (PDF) for each object given the best-fit values for the redshift and associated error produced by the REDMAGIC algorithm. We then obtain an overall estimate of the $n_g^i(z)$ of the samples by stacking these Gaussian probability distribution functions. We show the derived redshift distributions in Fig. 1, from which it can be seen that the number of galaxies increases with redshift at low redshift because of the increasing volume and decreases thereafter due to the brighter luminosity cuts imposed.

As done in [54], the galaxy mask is constructed from the REDMAGIC galaxy catalog over the SPT contiguous region by excluding areas outside the survey footprint, bad-quality regions, and pixels with an observed coverage fraction smaller than 80%. For the pixels with coverage fraction above this threshold, we assign to each mask pixel i its coverage fraction f_i and use this value as a weight in the

[3]See Ref. [47].

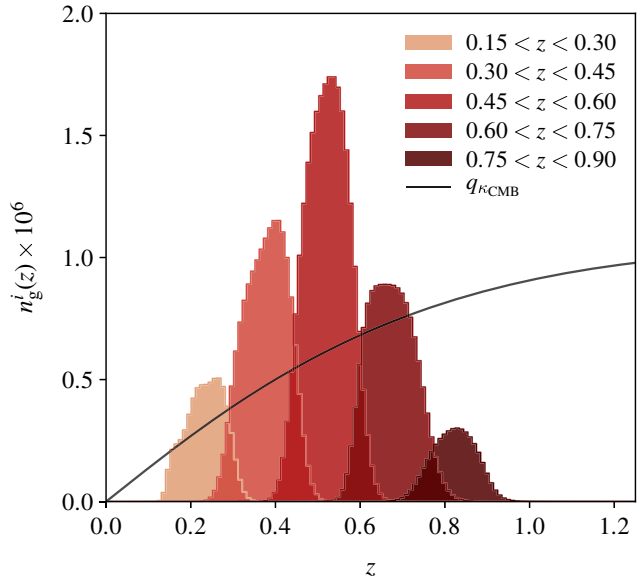


FIG. 1. Estimated redshift distribution of the REDMAGIC sample for the five tomographic bins used in this analysis. These are obtained by stacking Gaussian PDFs with mean equal to the REDMAGIC redshift prediction and standard deviation equal to the resulting redshift error. Each distribution is normalized to give the total number of galaxies in each bin. The CMB lensing efficiency $q_{\kappa_{\rm CMB}}$ is shown in black for comparison.

clustering measurements that follow. In order to ensure the uniformity of the galaxy samples, we only use the fraction of the sky where the $L = 0.5(1.0, 1.5)L_*$ galaxy sample is complete up to $z = 0.6(0.75, 0.90)$. We multiply this mask with the $\kappa_{\rm CMB}$ mask, which results in a combined mask with an effective area of 1289 deg^2.

B. CMB lensing maps

The CMB weak lensing map used in this analysis is described by [15], and we give a brief description here. The lensing map is derived from an inverse variance weighted combination of SPT 150 GHz and Planck 143 GHz temperature data over the SPT-SZ survey region ($20^{\rm h}$ to $7^{\rm h}$ in right ascension and from $-65°$ to $-40°$ in declination; see, e.g., [56]).

Modes in this combined temperature map with $\ell < 100$ and $\ell > 3000$ are removed to avoid foreground contamination. Point sources in the flux density range $50 < F_{150} < 500$ mJy ($F_{150} > 500$ mJy) in the 150 GHz band are masked with an aperture of radius $6'$ ($9'$), while sources in the flux density range $6.4 < F_{150} < 50$ mJy are inpainted—the objects are masked and filled in with fluctuations similar to the CMB plus noise. Clusters from the SPT-detected sample of [57] with detection significance S/N > 6 are also masked with an aperture of $r = 5'$. The quadratic estimator technique [5] is then applied to the combined temperature map to reconstruct a filtered lensing map. Simulations are then used to debias and renormalize the amplitude of the lensing map. In constructing the lensing map, we use the lensing multipole range of $30 < \ell < 3000$ and apply a Gaussian smoothing of $\theta_{\rm FWHM} = 5.4'$ to the map. The low-pass filter is applied to suppress foreground contamination, while the high-pass filter is applied to remove modes we measure poorly in the data. When calculating the correlation functions, we apply an additional stricter mask that removes all the clusters with detection significance > 5 listed in [57] and DES REDMAPPER clusters with richness $\lambda > 80$ as well as point sources with flux density range $6.4 < F_{150} < 50$ mJy (which were inpainted prior to the reconstruction), in addition to that mask that was applied prior to the lensing reconstruction step.

By masking massive clusters in the CMB lensing map, we remove regions of high contamination by the thermal Sunyaev-Zel'dovich effect (tSZ) [58]. However, we also induce a secondary bias due to masking regions of high lensing convergence. It was shown in [44] that this secondary bias is small compared to other systematic effects such as tSZ.

IV. METHODS

We measure the clustering of the galaxies and their correlations with the CMB lensing maps in position space. Note that we take an approach slightly different from G16 here, and no smoothing is applied to the galaxy density maps. This smoothing only needs to be applied to the CMB lensing map in order to cut off the high level of noise that would otherwise leak from the high multipoles down to larger scales when transforming from harmonic to position space. The same smoothing was applied also to the galaxy overdensity maps in G16 for consistency, but this had the unwanted consequence of then spreading the shot-noise contribution (which in position space is normally confined to the zero-separation bin) out to larger angular separations, thus requiring a more complex modeling (see Appendix B of G16).

A. Correlation function

We measure both the autocorrelation of the galaxy density field and the cross-correlation between galaxies and $\kappa_{\rm CMB}$. The former is calculated using the Landy-Szalay estimator [59]:

$$w^{\delta_{\rm g}\delta_{\rm g}}(\theta_\alpha) = \frac{DD(\theta_\alpha) - 2DR(\theta_\alpha) + RR(\theta_\alpha)}{RR(\theta_\alpha)}, \quad (8)$$

with

$$DD(\theta_\alpha) = \frac{1}{N_{\theta_\alpha}^{DD}} \sum_{i=1}^{N_{\rm gal}} \sum_{j=1}^{N_{\rm gal}} \eta_i^D \eta_j^D \Theta_\alpha(\hat{\theta}^i - \hat{\theta}^j), \quad (9)$$

$$DR(\theta_\alpha) = \frac{1}{N_{\theta_\alpha}^{DR}} \sum_{i=1}^{N_{\rm gal}} \sum_{j=1}^{N_{\rm rand}} \eta_i^D \eta_j^R \Theta_\alpha(\hat{\theta}^i - \hat{\theta}^j), \quad (10)$$

$$RR(\theta_\alpha) = \frac{1}{N^{RR}_{\theta_\alpha}} \sum_{i=1}^{N_{\rm rand}} \sum_{j=1}^{N_{\rm rand}} \eta^R_i \eta^R_j \Theta_\alpha(\hat{\theta}^i - \hat{\theta}^j), \quad (11)$$

where η^D are the weights for the individual galaxies determined from cross-correlation with systematic maps (for randoms $\eta^R = 1$, see [54] for further details), N_θ are the total number of pairs of a given type [data-data (DD), data-random (DR), random-random (RR)] in a given angular bin θ_α, and $\Theta_\alpha(\hat{\theta}^i - \hat{\theta}^j)$ is 1 if a pair lies at an angular distance θ within the angular bin α and 0 otherwise. Random galaxies are generated uniformly over the union of the galaxy and $\kappa_{\rm CMB}$ masks and are included in the random catalog with probabilities matching the weight f_i at the pixel which the random galaxies fall onto.[4]

For the correlation function between a galaxy catalog and a pixellated map such as the CMB lensing convergence map, the correlation function is calculated using

$$w^{\delta_{\rm g}\kappa_{\rm CMB}}(\theta_\alpha) = D\kappa_{\rm CMB}(\theta_\alpha) - R\kappa_{\rm CMB}(\theta_\alpha), \quad (12)$$

with

$$D\kappa_{\rm CMB}(\theta_\alpha) = \frac{1}{N^{D\kappa_{\rm CMB}}_{\theta_\alpha}} \sum_{i=1}^{N_{\rm gal}} \sum_{j=1}^{N_{\rm pix}} \eta^D_i \eta^{\kappa_{\rm CMB}}_j \kappa_{{\rm CMB},j} \Theta_\alpha(\hat{\theta}^i - \hat{\theta}^j), \quad (13)$$

$$R\kappa_{\rm CMB}(\theta_\alpha) = \frac{1}{N^{R\kappa_{\rm CMB}}_{\theta_\alpha}} \sum_{i=1}^{N_{\rm rand}} \sum_{j=1}^{N_{\rm pix}} \eta^R_i \eta^{\kappa_{\rm CMB}}_j \kappa_{{\rm CMB},j} \Theta_\alpha(\hat{\theta}^i - \hat{\theta}^j), \quad (14)$$

where $\eta^{\kappa_{\rm CMB}}_j$ is the value of the mask and $\kappa_{{\rm CMB},j}$ is the value of convergence at the jth pixel.[5] In measuring the autocorrelation of galaxy density, we use 20 bins equally spaced in logarithm between $2.5' < \theta < 250'$; these angular bins are consistent with those of [54]. For $w^{\delta_{\rm g}\kappa_{\rm CMB}}(\theta)$, we use ten equally log-spaced angular bins over the same angular range due to the higher noise levels of this measurement. The measurements in both cases are carried out using the TreeCorr package [60].

Unlike G16, we do not perform a harmonic analysis in this paper since the other DES-Y1 two-point analyses are all conducted in position space, and our goal is to combine our measurements with those. We note that $C(\ell)$ estimators allow one to get a complementary understanding of systematics to those affecting the position-space estimators and are expected to yield consistent results in terms of significance of the cross-correlation signal and corresponding cosmological implications (as discussed in detail in G16).

[4]Here, we only consider the weights coming from the *galaxy* mask, although both the galaxy and $\kappa_{\rm CMB}$ masks are used to determine the valid pixels.

[5]Here, we only consider the weights coming from the $\kappa_{\rm CMB}$ mask, although both the galaxy and $\kappa_{\rm CMB}$ masks are used to determine the valid pixels.

B. Angular scale cuts

Our model for the correlation functions ignores several potential complications, such as the effects of tSZ bias in the CMB lensing map, the effects of nonlinear galaxy bias, and the effects of baryons on the matter power spectrum. In order to minimize biases to the inferred cosmological parameters in our analysis, we remove measurements at angular scales that we expect to be significantly impacted by these effects.

The choices of these angular scale cuts employed here were motivated for the analyses of $w^{\delta_{\rm g}\delta_{\rm g}}(\theta)$ and $w^{\delta_{\rm g}\kappa_{\rm CMB}}(\theta)$ in [44,46]. The scale cuts were determined by introducing unmodeled effects into simulated data vectors and performing simulated likelihood analyses to infer parameter biases. The scale cuts ultimately chosen in [44,46] were determined based on the joint analysis of two-point functions between the galaxy density, galaxy lensing and CMB lensing. Since the analysis of a single correlation function—such as $w^{\delta_{\rm g}\kappa_{\rm CMB}}(\theta)$—will necessarily be less constraining, by adopting these scale cuts in this analysis we are being conservative. It was shown in [44] that with these scale cuts, the bias on the cosmological parameter constraints will be less than 0.4σ, where σ represents the statistical uncertainty on the parameters.

The scale cut choices motivated by [44,46] result in removing from the galaxy-CMB lensing cross-correlation angular scales that are smaller than

$$\theta^{\delta_{\rm g}\kappa_{\rm CMB}}_{\rm min} = [15', 25', 25', 15', 15'] \quad (15)$$

for the five redshift bins. The corresponding scale cuts for the galaxy autocorrelations are [54]

$$\theta^{\delta_{\rm g}\delta_{\rm g}}_{\rm min} = [45', 25', 25', 15', 15']. \quad (16)$$

C. Covariance matrix

It was shown by G16 that several covariance matrix estimators (including a Gaussian analytic covariance in harmonic space) yield consistent results for the galaxy-CMB lensing correlation. Based on this comparison and the analysis of [46], we decided to use an analytic covariance estimate described in [46], but extended to include CMB lensing cross-correlations as described by [44]. Briefly, this estimator is a sum of Gaussian covariance and non-Gaussian terms based on a halo-model approach (which includes the trispectrum term and the supersample covariance). We additionally modify the term of this covariance that involves correlations between $\kappa_{\rm CMB}$ noise and $\delta_{\rm g}$ noise,

to take into account the survey geometry. This is done by replacing the analytic noise-noise covariance (which is calculated based on the galaxy number density and survey area only) with the covariance calculated from correlating Gaussian realizations of the $\kappa_{\rm CMB}$ map and the galaxy random catalog using the survey mask. This correction increases the diagonal elements of the analytic covariance by $\sim$10% for $w^{\delta_g\kappa_{\rm CMB}}(\theta)$. We compare this theoretical covariance estimate to a data-based jackknife estimate of the covariance in the Appendix.

D. Parameter constraints

The cross-correlation between galaxy density and the CMB convergence map contains cosmological information. To extract this information, we assume that the likelihood of the measured data vector $\vec{d}$ given a model $\vec{m}$ is Gaussian:

$$\ln \mathcal{L}(\vec{d}|\vec{m}(\vec{p})) = -\frac{1}{2}\sum_{ij}^{N}(d_i - m_i(\vec{p}))\mathbf{C}_{ij}^{-1}(d_j - m_j(\vec{p})), \tag{17}$$

where N is the number of points in the data and model vectors. The posteriors on the model parameters are given by

$$P(\vec{m}(\vec{p})|\vec{d}) \propto \mathcal{L}(\vec{d}|\vec{m}(\vec{p}))P_{\rm prior}(\vec{p}), \tag{18}$$

where $P_{\rm prior}(\vec{p})$ is the prior on the model parameters.

1. Galaxy bias and lensing amplitude constraints

Assuming the cosmological model is tightly constrained, joint measurement of $w^{\delta_g\kappa_{\rm CMB}}(\theta)$ and $w^{\delta_g\delta_g}(\theta)$ allows us to simultaneously constrain galaxy bias b and an overall multiplicative bias in the $\kappa_{\rm CMB}$ map, which we call A_κ. This is possible because the amplitude of the galaxy-CMB lensing cross-correlation scales with bA_κ, while the amplitude of the galaxy clustering correlation function scales with b^2.

We consider two scenarios along these lines while fixing the cosmological model to the fiducial model introduced in Sec. I. In the first scenario we fix $A_\kappa = 1$ and constrain the galaxy bias in each redshift bin while marginalizing over the photo-z uncertainties. The second scenario is identical to the first, but we let A_κ be free. In both cases we adopt the priors on systematics parameters presented in Table II.

2. Growth function

We use the measured correlation functions to constrain the cosmological growth function using two different methods. For both of these methods we assume $A_\kappa = 1$.

The first approach is the procedure introduced in G16 (also applied in [62]), which we compute here to compare with that analysis. For this method, we fix all the cosmological and nuisance parameters to the fiducial values listed in Table II. We define the growth-removed auto- and cross-spectra, indicated with a slashed symbol, via

TABLE II. The fiducial parameter values and priors for cosmological and nuisance parameters used in this analysis. Square brackets denote a flat prior over the indicated range, while parentheses denote a Gaussian prior of the form $\mathcal{N}(\mu,\sigma)$. The Gaussian priors on photo-z errors are determined by [61]. The fiducial cosmological parameter values are taken from the [41], but here we assume three massive neutrinos to stay consistent with other DES-Y1 analyses. For the photo-z bias, peaks of the posterior distributions in the DES joint galaxy clustering and lensing analysis [42] are used as fiducial values.

Parameter	Fiducial	Prior
Cosmology		
$\Omega_{\rm m}$	0.309	[0.1, 0.9]
$A_{\rm s}/10^{-9}$	2.14	[0.5, 5.0]
$n_{\rm s}$	0.967	[0.87, 1.07]
w	−1.0	Fixed
$\Omega_{\rm b}$	0.0486	[0.03, 0.07]
h_0	0.677	[0.55, 0.91]
$\Omega_\nu h^2$	6.45×10^{-4}	[0.0006, 0.01]
$\Omega_{\rm K}$	0	Fixed
τ	0.066	Fixed
Growth amplitude		
$A_{\rm D}$	1.0	[0.1, 4.0]
Lensing amplitude		
A_κ	1.0	[0.1, 4]
Galaxy bias		
b^i	1.45, 1.55, 1.65, 1.8, 2.0	[0.8, 3.0]
Lens photo-z error		
$\Delta^1_{z,{\rm g}}$	0.010	(0.008, 0.007)
$\Delta^2_{z,{\rm g}}$	−0.004	(−0.005, 0.007)
$\Delta^3_{z,{\rm g}}$	0.009	(0.006, 0.006)
$\Delta^4_{z,{\rm g}}$	0.001	(0.0, 0.01)
$\Delta^5_{z,{\rm g}}$	0.0	(0.0, 0.01)

$$\not{C}^{\delta_g\delta_g}(\ell) = \int d\chi \frac{q^i_{\delta_g}(\frac{\ell+\frac{1}{2}}{\chi},\chi)q^i_{\delta_g}(\frac{\ell+\frac{1}{2}}{\chi},\chi)}{\chi^2 D^2[z(\chi)]} P_{\rm NL}\left(\frac{\ell+\frac{1}{2}}{\chi}, z(\chi)\right), \tag{19}$$

$$\not{C}^{\delta_g\kappa_{\rm CMB}}(\ell) = \int d\chi \frac{q^i_{\delta_g}(\frac{\ell+\frac{1}{2}}{\chi},\chi)q_{\kappa_{\rm CMB}}(\chi)}{\chi^2 D^2[z(\chi)]} P_{\rm NL}\left(\frac{\ell+\frac{1}{2}}{\chi}, z(\chi)\right), \tag{20}$$

where $D(z)$ is the linear growth function. The angular power spectra are then transformed into $w(\theta)$ using Eq. (6),

and our growth estimator is given by the ratio between[6] the observed and theoretical slashed correlation functions, averaged over a range of angular scales $[\theta^{\rm min}_{D_{\rm G}}, \theta^{\rm max}_{D_{\rm G}}]$:

$$D_{\rm G} = \left\langle \frac{w^{\delta_{\rm g}\kappa_{\rm CMB}}_{\rm observed}(\theta)}{w^{\delta_{\rm g}\kappa_{\rm CMB}}_{\rm theoretical}(\theta)} \sqrt{\frac{w^{\delta_{\rm g}\delta_{\rm g}}_{\rm theoretical}(\theta)}{w^{\delta_{\rm g}\delta_{\rm g}}_{\rm observed}(\theta)}} \right\rangle_{\theta^{\rm min}_{D_{\rm G}}<\theta<\theta^{\rm max}_{D_{\rm G}}} . \quad (21)$$

We measure this quantity for the five tomographic bins, which allows us to measure the evolution of the growth function in redshift bins [i.e., $D_{\rm G}(z_i)$]. The advantage of this estimator is that the measured quantity is independent of galaxy bias since bias is canceled out by taking the ratio. Due to the filtering that removes $\ell < 30$ in the $\kappa_{\rm CMB}$ map, the fiducial model $w^{\delta_{\rm g}\kappa_{\rm CMB}}_{\rm theoretical}(\theta)$ reaches zero near $\theta = 100'$, so we restrict our measurements to scales $\theta < \theta^{\rm max}_{D_{\rm G}} = 100'$. For $\theta^{\rm min}_{D_{\rm G}}$, we conservatively choose the larger scale between the auto- and cross-correlation scale cuts of Sec. IV B for each redshift bin.

In order to test for possible deviations from the baseline ΛCDM model across the five redshift bins, we assume the shape of the linear growth function $D(z)$ to be fixed by the fiducial cosmology, and we fit for a redshift-independent quantity $A_{\rm D}$ such that it minimizes:

$$\chi^2 = \sum_{ij}^{5} (D_{\rm obs}(z_i) - A_{\rm D} D_{\rm fid}(z_i)) \mathbf{C}^{-1}_{ij} (D_{\rm obs}(z_j) - A_{\rm D} D_{\rm fid}(z_j)), \quad (22)$$

with $D_{\rm obs}(z_i) \equiv D_{\rm G}$ for this method. We take 50 000 multivariate Gaussian draws from the analytical covariance matrix to produce simulated $w^{\delta_{\rm g}\delta_{\rm g}}(\theta)$ and $w^{\delta_{\rm g}\kappa_{\rm CMB}}(\theta)$ data vectors, calculate $D(z)$ for each draw, and compute the covariance matrix $\mathbf{C}_{ij}$ over the ensemble of realizations.

The second method for measuring the growth function consists of simultaneously fitting $A_{\rm D}$, galaxy bias, and photo-z bias to the observed auto- and cross-correlations using a Markov chain Monte Carlo (MCMC) approach. This method has an advantage of allowing us to vary over other systematic effects, such as photo-z errors. For this method, we fix the cosmological parameters to the fiducial values in Table II but vary the growth amplitude, galaxy biases and lens photo-z biases over the priors given in the same table.

3. Cosmological parameter estimation

Finally, we use the measurements of both $w^{\delta_{\rm g}\kappa_{\rm CMB}}$ and $w^{\delta_{\rm g}\delta_{\rm g}}$ presented in this work to constrain cosmological parameters. We generate posterior samples using the MULTINEST algorithm [63] as implemented in the COSMOSIS [64] package. We let the photo-z bias [i.e., lens $n(z)$ shift], galaxy bias and six cosmological parameters ($\Omega_{\rm m}$, $A_{\rm s}$, $n_{\rm s}$, $\Omega_{\rm b}$, h, Ω_ν) vary simultaneously, while we fix $A_\kappa = A_{\rm D} = 1$. Here, $A_{\rm s}$ is the amplitude of the matter power spectrum, $n_{\rm s}$ is the spectral index, $\Omega_{\rm b}$ is the baryon density, h is the unitless Hubble constant and Ω_ν is the neutrino density. Priors on these parameters are summarized in Table II. In this study we will focus on the constraints on $\Omega_{\rm m}$ and $S_8 \equiv \sigma_8\sqrt{\Omega_{\rm m}/0.3}$, where σ_8 is the rms amplitude of mass fluctuations on $8h^{-1}$ Mpc scale. S_8 is defined to be approximately the most constrained cosmological parameter combination for galaxy weak lensing measurements.

[6]This ratio only works in the limit when the redshift slices are narrow.

E. Blinding

This analysis was blinded throughout the study using a combination of various blinding schemes. First, the analysis pipeline was built using FLASK simulations and the paper was originally written assuming these data vectors. We then switched to a scheme where we multiplied the CMB lensing map by an unknown factor in the range between 0.8 and 1.2 and shifted the cosmological parameter constraints that we obtained by an arbitrary number and removed the axes when generating figures. After the data passed all systematic checks, the measurements were repeated using a CMB lensing map without the random factor applied, and the cosmological parameter constraints were calculated without shifts.

V. SYSTEMATIC ERROR ANALYSIS

Systematic errors can impact the relationship between the measured and predicted correlation functions in three ways: (i) by affecting the observed density of galaxies on the sky, (ii) by affecting the CMB lensing map, and (iii) by affecting the inferred redshift distributions of the galaxies. Systematics affecting the observed density of DES REDMAGIC galaxies were explored by [54] as part of the [42] analysis. The main source of systematic error impacting the CMB lensing map is contamination by the tSZ effect which has been discussed and modeled in [44]. Systematic errors in the photometric redshift distributions of REDMAGIC galaxies were explored by [61], also as part of the [42] analysis. Below, we draw heavily from these companion papers to constrain the systematic contamination of the measured correlation functions.

A. Galaxy density and CMB lensing biases

We first consider systematics impacting galaxy density and the CMB lensing map. It is useful to divide these systematics into two categories: those that produce a bias that is uncorrelated with the true density fluctuations and those that produce a bias that is correlated with them. For those systematic biases that are uncorrelated with the true density fluctuations, in order to generate a bias in $w^{\delta_{\rm g}\kappa_{\rm CMB}}$, the systematic must contaminate *both* the galaxy density and $\kappa_{\rm CMB}$; if it only impacts one of these observables, its

impact on the correlation function should average to zero. One of the strengths of cross-correlation measurements such as $w^{\delta_g\kappa_{CMB}}$ is that there are not many systematics that could contaminate both of the observed fields. However, there are some potential sources of bias that could do this. One example is dust, which is one of the foreground components of the CMB temperature measurements, and one can expect potential residuals in a single-frequency temperature map that can then propagate into the CMB lensing map. Dust also affects the photometry of the observed galaxies and is correlated with galactic latitude. This contamination can then induce density fluctuations through the change of mean density with latitude. Consequently, dust extinction may contaminate simultaneously galaxy density and CMB lensing and could therefore contaminate measurement of $w^{\delta_g\kappa_{CMB}}$. In what follows we will consider dust extinction and stellar density maps as potential contaminants.

On the other hand, there are some sources of contamination which *are* correlated with the true density fluctuations. In this case, the contaminant needs not affect both galaxy density and CMB lensing in order to bias $w^{\delta_g\kappa_{CMB}}(\theta)$. At ∼150 GHz (roughly the frequencies of the SPT and *Planck* maps used to generate the CMB lensing map), the tSZ effect results in a decrement in the observed CMB temperature around clusters. This non-Gaussian feature gets picked up as a false lensing signal by the quadratic estimator. Since hot gas is correlated with galaxies, we expect the tSZ effect to induce a bias in the measured correlation functions. The cosmic infrared background (CIB), which is dominated by emission from dusty star forming galaxies, is another extragalactic foreground that injects non-Gaussian features in our temperature maps. While the CIB emission spectrum peaks at a higher frequency, minor correlations with 150 GHz observations are expected, which again lead to a false lensing signal. Since both the CIB and tSZ originate from large-scale structure, we expect them to introduce biases in κ_{CMB} that are correlated with density fluctuations. Maps for both tSZ and CIB contamination are built and described in detail by [44]. That work also identified the tSZ effect as the dominant source of systematic affecting the cross-correlation measurement between κ_{CMB} and δ_g. While the angular scale cuts proposed by [44] and restated in Sec. IV B are chosen to mitigate these biases, they do not remove them entirely, and the residuals must be quantified.

Of all the systematic effects that could potentially be present in our maps and catalogs, only the ones which are correlated with *both* the observed CMB lensing map and the galaxy catalog affect our cross-correlation measurements. We can therefore measure the quantity

$$\frac{w^{\kappa^{obs}_{CMB}\mathcal{S}}(\theta)w^{\delta^{obs}_g\mathcal{S}}(\theta)}{w^{\mathcal{S}\mathcal{S}}(\theta)} \tag{23}$$

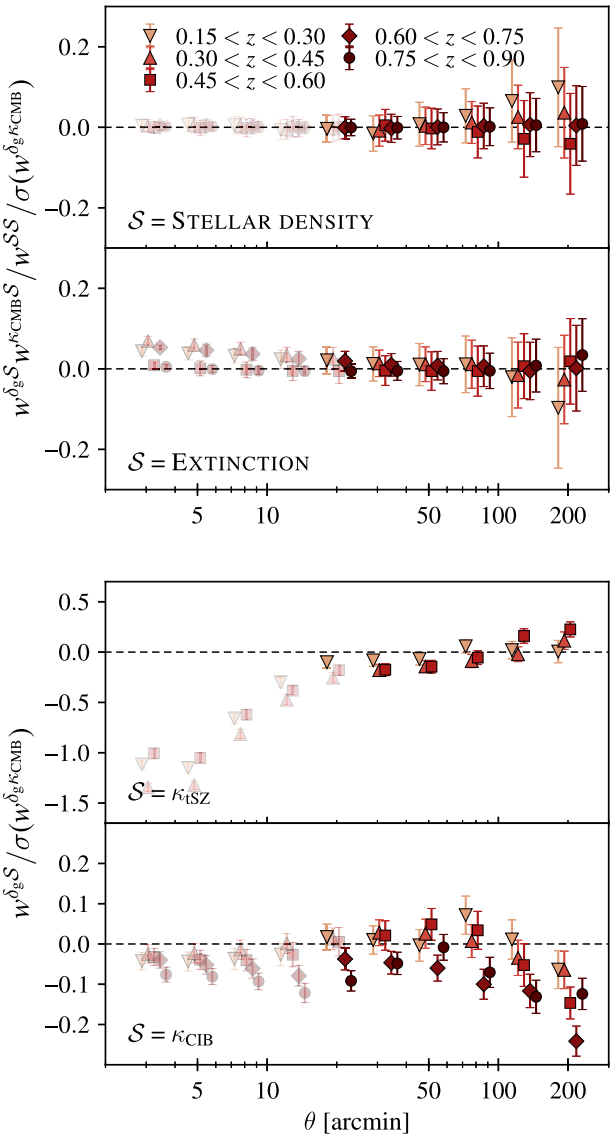


FIG. 2. Top two panels: Contributions due to uncorrelated systematics to the galaxy-CMB lensing cross-correlations, as described by Eq. (23), in units of the statistical errors on the observed cross-correlation. Lower two panels: Contributions due to correlated systematics, given by the cross-correlations between the κ_{CMB} systematics (κ_{tSZ} and κ_{CIB}) and δ_g, also in units of the statistical error. We observe that within the angular scales we consider the ratios are < 1 for all redshift bins for all systematic maps (the faded points are removed from the analysis due to the imposed scale cuts). Since the tSZ template is generated only using REDMAPPER clusters up to $z = 0.6$, the correlations for the higher two redshift bins have been ignored (see [44]). Note the different scales used for κ_{tSZ} and κ_{CIB}.

to quantify the amplitude of the bias (to first order), which we expect to be zero for systematic maps that are not correlated with both the CMB lensing map and galaxy catalogs. However for astrophysical systematic effects such as tSZ and CIB which could potentially be contaminating the CMB temperature map, physical correlations with κ^{true}_{CMB}

are expected, and therefore Eq. (23) is not expected to equal 0. Therefore, for these systematic effects, we directly measure the correlations $w^{\delta_g\kappa_{\rm tSZ}}(\theta)$ and $w^{\delta_g\kappa_{\rm CIB}}(\theta)$ to quantify the bias. As described in more detail in [44], we estimate $\kappa_{\rm tSZ}$ by passing a template tSZ map through the lensing pipeline of [15]; similarly, $\kappa_{\rm CIB}$ is estimated by passing a 545 GHz CIB map [65] though the [15] lensing pipeline.

We first focus on those systematics that are uncorrelated with the true density. We show in the top half of Fig. 2 the ratio between $w^{\kappa_{\rm CMB}\mathcal{S}}(\theta)w^{\delta_g\mathcal{S}}(\theta)/w^{\mathcal{SS}}(\theta)$ measured for dust extinction and stellar contamination and the uncertainty on the measured galaxy density-CMB lensing correlation and verify that this ratio is significantly smaller than 1 and consistent with 0 across all angular scales. We can see that the impact on the measurements is generally small compared with the statistical error bars, so that we can conclude there is no evidence for any of these contaminants making a significant impact on our results.

We then consider the correlated sources of systematics: tSZ and CIB, and we show their contributions to Eq. (23) in the bottom half of Fig. 2. Here we indeed see nonzero residuals coming from tSZ but most of this bias is removed by applying our default scale cuts, and the remaining bias is within 0.35σ, where σ is the statistical uncertainty.

We note that [54] investigated the impact of several observational systematics in addition to dust extinction and stellar density that could introduce spurious fluctuations in REDMAGIC galaxy number density on large scales. Using a set of 20 survey property maps,[7] in addition to stellar contamination and galactic extinction, they studied the dependence of number density as a function of these observational properties. The results of these tests indicated that REDMAGIC galaxies were not largely impacted by these systematics. Furthermore, as mentioned above, since we do not expect the DES-specific survey systematics (exposure time, sky brightness, air mass, seeing, survey depth variations) to correlate with $\kappa_{\rm CMB}$, we do not expect these to bias $w^{\delta_g\kappa_{\rm CMB}}(\theta)$.

B. Photo-z systematics

Unlike biases in the galaxy density or CMB lensing maps, we explicitly model biases in the estimated redshift distributions of the galaxies as described in Sec. II.

The [42] analysis constrained biases in the inferred redshift distributions of the REDMAGIC galaxies using angular cross-correlations with spectroscopic data from the Sloan Digital Sky Survey (DR8), particularly Baryon Oscillation Spectroscopic Survey luminous red galaxies. This analysis is presented in [61]. These resultant priors on the photo-z bias parameters $\Delta^i_{z,g}$ for the five redshift bins are listed in Table II. We let these values vary when calculating the growth amplitude and cosmological parameter constraints in Secs. VI B 2 and VI C.

VI. RESULTS

We show in Fig. 3 the measured autocorrelation functions of the REDMAGIC galaxy sample and its cross-correlation with the SPT + *Planck* CMB lensing map. The small-scale data points shown with faded symbols are the scales removed by the scale cuts as discussed in Sec. IV B. The theoretical predictions assuming the fiducial cosmology listed in Table II are shown as the black lines. In the following sections we extract cosmological information using these measurements.

We note that we made few modifications in Secs. VI A and VI B after we unblinded the data. We first added constraints on the galaxy bias from $w^{\delta_g\kappa_{\rm CMB}}(\theta)$ alone with the cosmology fixed to *Planck* best-fit values (instead of DES-Y1). The motivation for this was to allow us to directly compare the constraints on galaxy bias when varying over the cosmological parameters, but combining with the *Planck* baseline likelihood. Accordingly, we also changed the assumed cosmology when computing the best-fit biases from $w^{\delta_g\delta_g}(\theta) + w^{\delta_g\kappa_{\rm CMB}}(\theta)$. Additionally, we recomputed the galaxy biases inferred from galaxy clustering and galaxy-galaxy lensing using the same data vectors but combined with *Planck* baseline likelihood.

A. Galaxy bias and lensing amplitude

We first fix the cosmological parameters to the fiducial values and vary the galaxy bias and lens photo-z error parameters simultaneously, imposing the priors shown in Table II. We focus on constraining galaxy bias, assuming a fixed lensing amplitude of $A_\kappa = 1$. When using both $w^{\delta_g\delta_g}(\theta)$ and $w^{\delta_g\kappa_{\rm CMB}}(\theta)$, we obtain $b^1 = 1.47^{+0.08}_{-0.08}$, $b^2 = 1.67^{+0.06}_{-0.04}$, $b^3 = 1.68^{+0.04}_{-0.04}$, $b^4 = 2.03^{+0.04}_{-0.05}$, and $b^5 = 2.14^{+0.05}_{-0.08}$, with $\chi^2 = 107.3$ for 82 data points. The high value of χ^2 is primarily driven by the galaxy clustering measurements (see [54]).

When we additionally treat the CMB lensing amplitude A_κ as a free parameter, we obtain $b^1 = 1.46^{+0.09}_{-0.07}$, $b^2 = 1.68^{+0.06}_{-0.05}$, $b^3 = 1.68^{+0.04}_{-0.04}$, $b^4 = 2.02^{+0.05}_{-0.04}$, and $b^5 = 2.12^{+0.08}_{-0.06}$. The recovered posterior on the lensing amplitude is $A_\kappa = 1.00^{+0.16}_{-0.09}$, with a total $\chi^2 = 107.2$. The similarity between the constraints on the galaxy bias values that we obtain with A_κ fixed to 1 and free suggests that the galaxy bias constraints in this analysis are dominated by $w^{\delta_g\delta_g}(\theta)$. These results are summarized in Table III.

Next, we consider constraints on galaxy bias from $w^{\delta_g\kappa_{\rm CMB}}(\theta)$ alone. We reject the hypothesis of no lensing with a significance[8] of 19.9σ when no scale cuts are

[7] These were exposure time, sky brightness, air mass, seeing and survey 10σ depth, in four different broad bands.

[8] The significance is calculated using $\sqrt{\chi^2_{\rm null}}$, where $\chi^2_{\rm null}$ is the value of χ^2 computed under the null model, i.e., with galaxy bias $b = 0$.

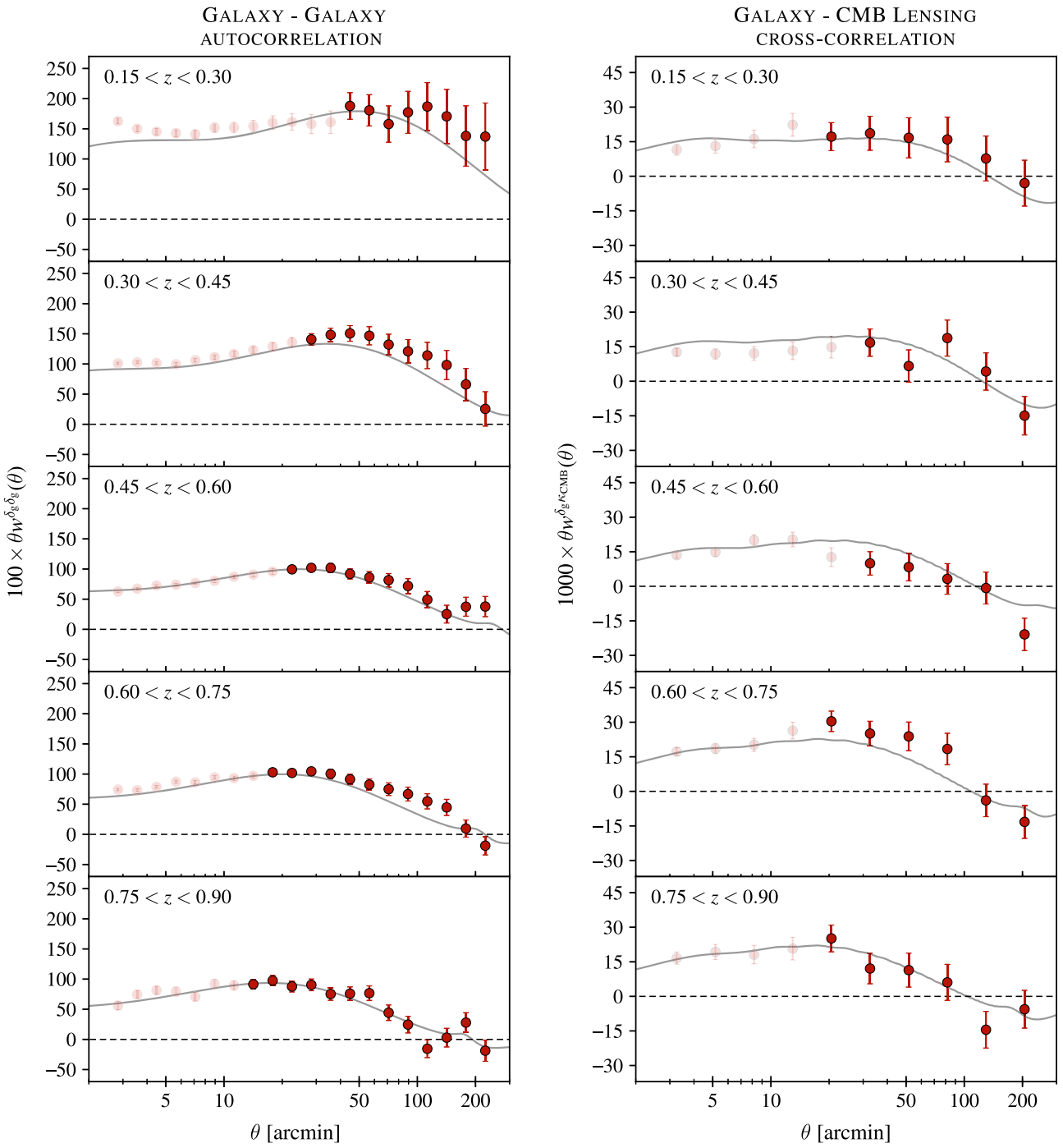


FIG. 3. Measured auto- and cross-correlation functions between the REDMAGIC galaxy sample described in Sec. III A and CMB lensing from [15]. The faint angular bins have been excluded from the fits, consistently with [54] and with [44]. The theory modeling shown uses the mean bias and cross-correlations amplitudes found in Sec. VI and Table III, assuming the fiducial cosmology listed in Table II. The error bars shown are the diagonal elements of the covariance matrix $\sqrt{\mathbf{C}_{ii}}$, and therefore, the correlations between the bins are ignored. In contrast, the best-fit amplitudes are calculated including the off-diagonal elements and therefore the best-fit lines and data points may not match visually in certain bins.

imposed and 9.9σ after imposing scale cuts. The constraints on galaxy bias from this analysis are summarized in Table IV. Not surprisingly, the constraints on galaxy bias from $w^{\delta_g\kappa_{\rm CMB}}(\theta)$ alone are significantly weaker than in the case when the measurements are combined with $w^{\delta_g\delta_g}(\theta)$. Similar constraints on galaxy biases are obtained when

TABLE III. Summary of the constraints on the galaxy bias parameters using $w^{\delta_g\delta_g}(\theta) + w^{\delta_g\kappa_{CMB}}(\theta)$ and assuming *Planck* best-fit ΛCDM cosmology. We consider two cases: fixing the lensing amplitude to 1 (left) and setting A_κ free (right). We obtain χ^2 of 107.3 and 107.2, respectively, for 82 data points. Since most of the constraining power is coming from $w^{\delta_g\delta_g}(\theta)$, we find similar values for the galaxy biases for the two cases. The difference between the values reported here and in [54] is due to the cosmology assumed.

Sample	Bias ($A_\kappa = 1$)	Bias ($A_\kappa \neq 1$)
$0.15 < z < 0.30$	$1.47^{+0.08}_{-0.08}$	$1.46^{+0.09}_{-0.07}$
$0.30 < z < 0.45$	$1.67^{+0.06}_{-0.04}$	$1.68^{+0.06}_{-0.05}$
$0.45 < z < 0.60$	$1.68^{+0.04}_{-0.04}$	$1.68^{+0.04}_{-0.04}$
$0.60 < z < 0.75$	$2.03^{+0.04}_{-0.05}$	$2.02^{+0.05}_{-0.04}$
$0.75 < z < 0.90$	$2.14^{+0.05}_{-0.08}$	$2.12^{+0.08}_{-0.06}$
		$A_\kappa = 1.00^{+0.16}_{-0.09}$

TABLE IV. Summary of the constraints on the galaxy bias parameters from $w^{\delta_g\kappa_{CMB}}(\theta)$ only with fixed cosmology and in combination with the *Planck* baseline likelihood. In both cases photo-z biases are varied over with the priors from [42]. The χ^2 that we obtain are 27.6 and 26.1 for 27 data points.

Sample	Fixed	+*Planck* baseline
$0.15 < z < 0.30$	$1.54^{+0.44}_{-0.38}$	$1.47^{+0.51}_{-0.38}$
$0.30 < z < 0.45$	$1.45^{+0.33}_{-0.42}$	$1.30^{+0.46}_{-0.32}$
$0.45 < z < 0.60$	$1.10^{+0.36}_{-0.21}$	$1.06^{+0.34}_{-0.20}$
$0.60 < z < 0.75$	$2.69^{+0.23}_{-0.28}$	$2.78^{+0.17}_{-0.35}$
$0.75 < z < 0.90$	$2.17^{+0.45}_{-0.42}$	$2.31^{+0.35}_{-0.52}$

cosmological parameters are varied, but cosmological priors from *Planck* baseline likelihood are imposed (right column of Table IV).

The bias constraints from $w^{\delta_g\kappa_{CMB}}(\theta)$, as well as those from the DES-Y1 galaxy clustering [54] and galaxy-galaxy lensing analyses [66] when combined with *Planck* baseline likelihood, are shown in Fig. 4. We find that considerably tighter constraints can be obtained from $w^{\delta_g\delta_g}(\theta)$ relative to $w^{\delta_g\gamma_t}(\theta)$ and $w^{\delta_g\kappa_{CMB}}(\theta)$. The constraining power of $w^{\delta_g\kappa_{CMB}}(\theta)$ relative to $w^{\delta_g\gamma_t}(\theta)$ increases with higher redshift galaxy samples. This is because the number of available background galaxies decreases as we increase the redshift of the lens galaxy sample. In contrast, the signal improves for $w^{\delta_g\kappa_{CMB}}(\theta)$ due to the better overlap with the CMB lensing kernel as shown in Fig. 1.

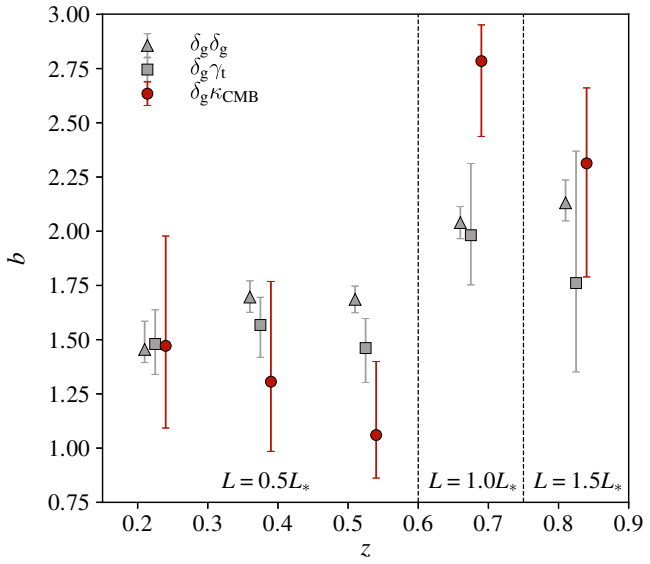


FIG. 4. Galaxy bias estimation of REDMAGIC galaxies from different probes, as a function of redshift when combined with *Planck* baseline likelihood. The results from $w^{\delta_g\kappa_{CMB}}(\theta)$ assuming $A_\kappa = 1$ are shown in red. Additionally plotted are the measurements from galaxy clustering [54] (gray triangles) and galaxy-galaxy lensing [66] (gray squares).

B. Growth constraints

Next, we study the broader cosmological implications of our measurement: we first assume cosmology to be fixed at high redshift, e.g., by the *Planck* CMB observations, and test whether the linear growth function inferred from our measurement at low redshift is consistent with the baseline ΛCDM model predictions. We test this using the two methods described in Sec. IV D 2.

1. The D_G estimator

We first measure the linear growth function $D(z)$ using the D_G estimator. We compute D_G for all five tomographic bins, applying the conservative angular scale cuts listed in Sec. IV B and additionally removing scales above 100′ (see Sec. IV D 2 for details). The results are shown in Fig. 5. In addition, we also calculate the best-fit amplitude A_D by combining all the bins, from which we obtain $A_D = 1.16^{+0.20}_{-0.20}$, which agrees with the fiducial ΛCDM expectation of $A_D = 1$.

In comparing the result presented here (using 1289 deg^2) with that of G16 that used DES-SV data covering 140 deg^2, we see that we obtain similar constraining power. This is due to

(1) the conservative scale cuts imposed in this study to minimize $w^{\delta_g\kappa_{tSZ}}(\theta)$ bias,
(2) the lower number density of REDMAGIC than the galaxy sample used by G16, in exchange for better photo-z errors, and

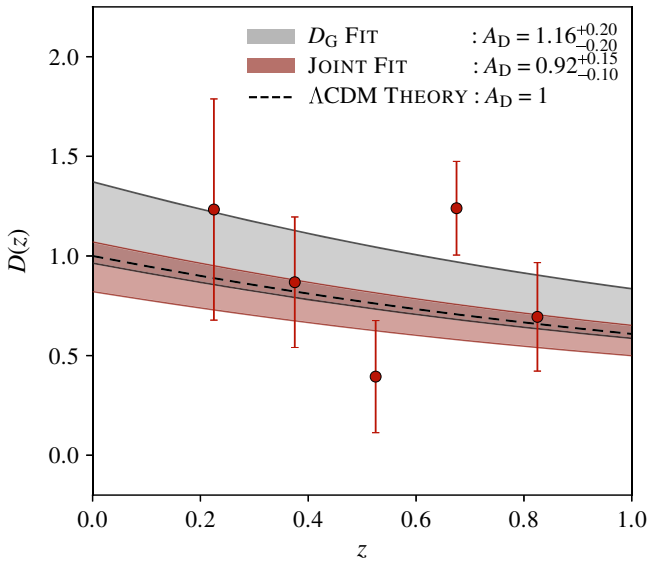


FIG. 5. Growth function estimates from the combination of auto- and cross-correlation functions, at the fiducial cosmology. The red points show the measured value of D_G in each redshift bin, with error bars representing the diagonal elements of the covariance matrix described in Sec. IV D 2. The gray band represents the 1σ confidence interval on the best-fit amplitude A_D, assuming the fiducial ΛCDM template shown in black (solid), and the red shaded regions describe the 1σ uncertainties from the joint-fit analysis described in Sec. VI B 2.

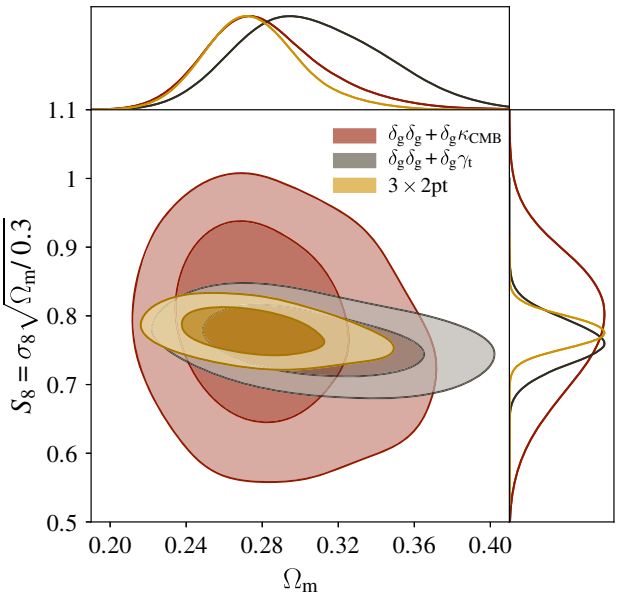


FIG. 6. Constraints on Ω_m and S_8 from the measurements of this paper and combinations of other two-point correlation functions. We show the constraints from $w^{\delta_g\delta_g}(\theta) + w^{\delta_g\kappa_{CMB}}(\theta)$ (red), $w^{\delta_g\delta_g}(\theta) + w^{\delta_g\gamma_t}(\theta)$ (gray) and 3×2 point (gold).

(3) the lower temperature ℓ_{max} used ($\ell_{max} = 3000$) in the lensing reconstruction process in [15] to avoid contamination by astrophysical foregrounds (whereas the SPT lensing map used in the G16 analysis had $\ell_{max} = 4000$).

Therefore, we have exchanged signal-to-noise ratio with increased robustness of the measurement.

We have tested that the general scale cuts used by [44] are also appropriate for the D_G estimator. We have confirmed this by running the estimator on contaminated theory data vectors, for which we found that the bias on the recovered growth is always $< 0.5\sigma$ if the standard scale cuts of Sec. IV B are used. This is not the case for less conservative cuts, which we therefore discard: for example, using the full range of scales down to $2'$ biases D_G at the 2σ level. The bias at small angular scales is mainly driven by the tSZ contamination in the CMB lensing map, as discussed in [44].

2. Joint growth fit results

Here we keep the cosmological parameters fixed to the fiducial model but marginalize over the five independent linear galaxy bias parameters (one for each redshift bin), the photo-z uncertainties and the linear growth parameter A_D using the priors presented in Table II. We measure the linear galaxy bias to be $b^1 = 1.45^{+0.30}_{-0.15}$, $b^2 = 1.73^{+0.26}_{-0.22}$, $b^3 = 1.80^{+0.17}_{-0.29}$, $b^4 = 2.04^{+0.35}_{-0.21}$, and $b^5 = 2.15^{+0.36}_{-0.24}$ and find a constraint of $A_D = 0.92^{+0.15}_{-0.10}$ for the amplitude of the growth function. These measurements of the bias are in agreement with the results shown in Table III. The recovered growth function agrees with the fiducial ΛCDM expectation, as the measurement of A_D is consistent with 1.0. We observe that the errors on the galaxy bias are larger compared to a direct best-fit estimation presented in Sec. VI A. This is due to the fact that the bias and A_D parameters are correlated. In turn, the fact that the joint-fit method gets a different value of A_D with respect to the D_G method is because it explicitly takes into account the correlations between bias and growth.

C. Cosmological parameter estimation

In this section, we present the full cosmological analysis using the $w^{\delta_g\delta_g}(\theta) + w^{\delta_g\kappa_{CMB}}(\theta)$ data vectors and marginalizing over all the cosmological parameters and nuisance parameters (galaxy bias and photo-z bias, but we fix $A_D = A_\kappa = 1$).

The priors used in this analysis are summarized in Table II and are the same as used in [42] to maintain consistency between the analyses.

In Fig. 6 we show the constraints obtained on matter density Ω_m and S_8 when all six cosmological parameters, photo-z errors and linear galaxy biases for the five redshift bins are marginalized over. This is then compared with the constraints from the combination of $w^{\delta_g\delta_g}(\theta) + w^{\delta_g\gamma_t}(\theta)$ as presented in [42]. We observe that these two measurements

slice through the parameter space slightly differently. Using $w^{\delta_g\delta_g}(\theta) + w^{\delta_g\kappa_{CMB}}(\theta)$ we obtain $\Omega_m = 0.276^{+0.029}_{-0.030}$ and $S_8 = 0.800^{+0.090}_{-0.094}$, whereas the combination of $w^{\delta_g\delta_g}(\theta) + w^{\delta_g\gamma_t}(\theta)$ gives us $\Omega_m = 0.294^{+0.047}_{-0.029}$ and $S_8 = 0.759^{+0.037}_{-0.031}$. These two results can also be compared with the constraints from 3×2 point [the combination of $w^{\delta_g\delta_g}(\theta) + w^{\delta_g\gamma_t}(\theta) + \xi_{+/-}(\theta)$] [42], which gives $\Omega_m = 0.267^{+0.030}_{-0.017}$ and $S_8 = 0.773^{+0.026}_{-0.020}$. These results are highly consistent with each other as shown in Fig. 6.

The measurement used in this analysis are combined with the $w^{\gamma_t\kappa_{CMB}}(\theta)$ presented in [43] and the results from [42] in [45], using the methodology outlined in [44].

VII. CONCLUSIONS

We have presented measurements of the DES REDMAGIC galaxy-CMB lensing cross-correlation as a function of redshift. Our measurement rejects the hypothesis of no lensing at 19.9σ[9] significance prior to any scale cuts and 9.9σ using the conservative scale cuts from [44]. The conservative scale cuts reduce the signal to noise of the measurements in exchange for mitigation of systematic biases.

We test for the impact of possible systematics in the cross-correlations, considering contaminants to both the DES galaxy and the CMB lensing maps. We find that, on the scales we consider, all these contaminants have a small impact on our measurements compared with the statistical uncertainties. The largest effect comes from the tSZ contribution to the CMB lensing maps, which becomes large at smaller angular scales, and is the main limiting factor dictating our scale cuts [44]. Improving the modeling and subtraction of this contaminant will be the key to extracting the full statistical power of the temperature-based CMB lensing maps in the future.

In obtaining the galaxy bias parameters, we find that galaxy-clustering measurements place significantly tighter constraints than galaxy-galaxy lensing or galaxy-CMB lensing correlations. However, the two cross-correlations are nonetheless important in breaking degeneracies in parameter space.

We use our measurements to infer cosmological information in a number of ways. We first constrain the linear growth function using the D_G estimator introduced by G16, finding a relative growth amplitude of $A_D = 1.16^{+0.20}_{-0.20}$. This compiles measurements of growth in various tomographic bins, accounting for their covariance. We then extend this result and constrain the relative growth amplitude with a joint-fit method, marginalizing over galaxy biases and photo-z uncertainties and considering the full covariance of the observables. In this case, we find $A_D = 0.92^{+0.15}_{-0.10}$. Both of these results are consistent with the ΛCDM predictions of $A_D = 1$.

Using these measurements, we finally run a full MCMC analysis over the ΛCDM cosmological parameters to also place marginalized constraints on the two parameters that are most directly related to the matter density field: Ω_m and $S_8 \equiv \sigma_8\sqrt{\Omega_m/0.3}$. Using the combination of $w^{\delta_g\delta_g}(\theta)$ and $w^{\delta_g\kappa_{CMB}}(\theta)$ we obtain $\Omega_m = 0.276^{+0.029}_{-0.030}$ and $S_8 = 0.800^{+0.090}_{-0.094}$. This can be compared with the results obtained using galaxy clustering and galaxy-galaxy lensing [i.e., $w^{\delta_g\delta_g}(\theta) + w^{\delta_g\gamma_t}(\theta)$], which gives $\Omega_m = 0.294^{+0.047}_{-0.029}$ and $S_8 = 0.759^{+0.037}_{-0.031}$. We find that the constraining power is comparable despite the conservative scale cuts we have applied in this analysis, and we expect to obtain better signal in the future as we use galaxy samples at higher redshifts due to the better overlap with the CMB lensing kernel.

The constraining power of DES measurements of galaxy-CMB lensing correlations has the potential to improve in future analyses. The DES-Y3 will cover the full 5000 deg^2 of the DES footprint at approximately the same depth as Y1. Since the extended area does not overlap with the SPT footprint, we expect the gain in the signal to noise to be small in terms of improvements in sky coverage. However, our analysis choice in this study is conservative; we have chosen the scale cuts to minimize the biases in exchange for signal-to-noise ratio. To improve this measurement further, it will be essential to (i) characterize the bias to a higher accuracy, such that the signal loss is minimized, or (ii) improve the reconstruction of the CMB lensing map so that it is less prone to biases (see e.g., [67] for a discussion of modifications to temperature-based lensing reconstruction to minimize tSZ bias). Furthermore, newer datasets from SPT (SPTpol and SPT-3G [68]) have lower noise levels than SPT-SZ, and therefore, lensing maps generated from these datasets will have lower noise. Improvements along these lines will allow us to maximally extract the signal from this cross-correlation and to reach the best possible accuracy on cosmology.

[9]We note that while certain systematics could add to the apparent signal and artificially inflate the significance, in this case the main contamination without scale cuts is tSZ, which artificially reduces $w^{\delta_g\kappa_{CMB}}$. In other words, in the absence of tSZ and scale cuts, the significance of this measurement would be higher than 19.9σ.

ACKNOWLEDGMENTS

This paper has gone through internal review by the DES Collaboration. Y. O. acknowledges funding from the Kavli Foundation, the Natural Sciences and Engineering Research Council of Canada, Canadian Institute for Advanced Research, and Canada Research Chairs program. E. B. is partially supported by the U.S. Department of Energy Grant No. DE-SC0007901. C. C. was supported in

part by the Kavli Institute for Cosmological Physics at the University of Chicago through Grant No. NSF PHY-1125897 and an endowment from Kavli Foundation and its founder Fred Kavli. C. R. acknowledges support from a Australian Research Council Future Fellowship (FT150100074). B. B. is supported by the Fermi Research Alliance, LLC under Contract No. De-AC02-07CH11359 with the United States Department of Energy. The McGill authors acknowledge funding from the Natural Sciences and Engineering Research Council of Canada, Canadian Institute for Advanced Research, and Canada Research Chairs program. The South Pole Telescope program is supported by the National Science Foundation through Grant No. PLR-1248097. Partial support is also provided by the NSF Physics Frontier Center Grant No. PHY-0114422 to the Kavli Institute of Cosmological Physics at the University of Chicago, the Kavli Foundation, and the Gordon and Betty Moore Foundation through Grant No. GBMF#947 to the University of Chicago. This publication makes use of data products from the Wide-field Infrared Survey Explorer, which is a joint project of the University of California, Los Angeles, and the Jet Propulsion Laboratory/California Institute of Technology, funded by the National Aeronautics and Space Administration. Argonne National Laboratory's work was supported under U.S. Department of Energy Contract No. DE-AC02-06CH11357. Funding for the DES Projects has been provided by the U.S. Department of Energy, the U.S. National Science Foundation, the Ministry of Science and Education of Spain, the Science and Technology Facilities Council of the United Kingdom, the Higher Education Funding Council for England, the National Center for Supercomputing Applications at the University of Illinois at Urbana-Champaign, the Kavli Institute of Cosmological Physics at the University of Chicago, the Center for Cosmology and Astro-Particle Physics at the Ohio State University, the Mitchell Institute for Fundamental Physics and Astronomy at Texas A&M University, Financiadora de Estudos e Projetos, Fundação Carlos Chagas Filho de Amparo à Pesquisa do Estado do Rio de Janeiro, Conselho Nacional de Desenvolvimento Científico e Tecnológico and the Ministério da Ciência, Tecnologia e Inovação, the Deutsche Forschungsgemeinschaft and the Collaborating Institutions in the Dark Energy Survey. The Collaborating Institutions are Argonne National Laboratory, the University of California at Santa Cruz, the University of Cambridge, Centro de Investigaciones Energéticas, Medioambientales y Tecnológicas-Madrid, the University of Chicago, University College London, the DES-Brazil Consortium, the University of Edinburgh, the Eidgenössische Technische Hochschule (ETH) Zürich, Fermi National Accelerator Laboratory, the University of Illinois at Urbana-Champaign, the Institut de Ciències de l'Espai (IEEC/CSIC), the Institut de Física d'Altes Energies, Lawrence Berkeley National Laboratory, the Ludwig-Maximilians Universität München and the associated Excellence Cluster Universe, the University of Michigan, the National Optical Astronomy Observatory, the University of Nottingham, The Ohio State University, the University of Pennsylvania, the University of Portsmouth, SLAC National Accelerator Laboratory, Stanford University, the University of Sussex, Texas A&M University, and the OzDES Membership Consortium. Based in part on observations at Cerro Tololo Inter-American Observatory, National Optical Astronomy Observatory, which is operated by the Association of Universities for Research in Astronomy (AURA) under a cooperative agreement with the National Science Foundation. The DES data management system is supported by the National Science Foundation under Grants No. AST-1138766 and No. AST-1536171. The DES participants from Spanish institutions are partially supported by MINECO under Grants No. AYA2015-71825, No. ESP2015-66861, No. FPA2015-68048, No. SEV-2016-0588, No. SEV-2016-0597, and No. MDM-2015-0509, some of which include ERDF funds from the European Union. I. F. A. E. is partially funded by the CERCA program of the Generalitat de Catalunya. Research leading to these results has received funding from the European Research Council under the European Union's Seventh Framework Program (FP7/2007-2013) including ERC Grant Agreements No. 240672, No. 291329, and No. 306478. We acknowledge support from the Australian Research Council Centre of Excellence for All-sky Astrophysics (CAASTRO), through Project No. CE110001020, and the Brazilian Instituto Nacional de Ciência e Tecnologia (INCT) e-Universe (CNPq Grant No. 465376/2014-2). This manuscript has been authored by Fermi Research Alliance, LLC under Contract No. DE-AC02-07CH11359 with the U.S. Department of Energy, Office of Science, Office of High Energy Physics. The United States Government retains and the publisher, by accepting the article for publication, acknowledges that the United States Government retains a non-exclusive, paid-up, irrevocable, world-wide license to publish or reproduce the published form of this manuscript, or allow others to do so, for United States Government purposes. Computations were made on the supercomputer Guillimin from McGill University, managed by Calcul Québec and Compute Canada. The operation of this supercomputer is funded by the Canada Foundation for Innovation (CFI), the ministère de l'Économie, de la science et de l'innovation du Québec (MESI) and the Fonds de recherche du Québec—Nature et technologies (FRQ-NT). This research is part of the Blue Waters sustained-petascale computing project, which is supported by the National Science Foundation (Grants No. OCI-0725070 and No. ACI-1238993) and the state of Illinois. Blue Waters is a joint effort of the

University of Illinois at Urbana-Champaign and its National Center for Supercomputing Applications. We acknowledge the use of many python packages: ASTROPY, a community-developed core PYTHON package for astronomy [69], CAMB [49,70], COSMOSIS [71], GETDIST [72], HEALPIX [73], IPYTHON [74], MATPLOTLIB [75], NUMPY and SCIPY [76,77], QUICKLENS [78], and TREECORR [79].

APPENDIX: COVARIANCE MATRIX VALIDATION

Here we compare the analytical covariance matrix developed in [46] (and extended to include $\kappa_{\rm CMB}$ in [44]) with the data-based covariance obtained using the jackknife method.

From the data we compute the jackknife covariance as

$$C_{ij}^{\rm jk} = \frac{N_{\rm jk}-1}{N_{\rm jk}} \sum_{k}^{N_{\rm jk}} (\vec{d}^{\,k} - \bar{d})_i (\vec{d}^{\,k} - \bar{d})_j, \qquad \text{(A1)}$$

where $N_{\rm jk}$ is the number of jackknife patches used. Figure 7 shows the comparison between the jackknife and analytical covariances. We obtain diagonal covariance elements that are on average ∼17% higher than the analytical covariance over the angular scales of interest. Based on the discussion in [80,81], we consider that these are in sufficient agreement given that the jackknife method is a noisy estimate of the underlying covariance.

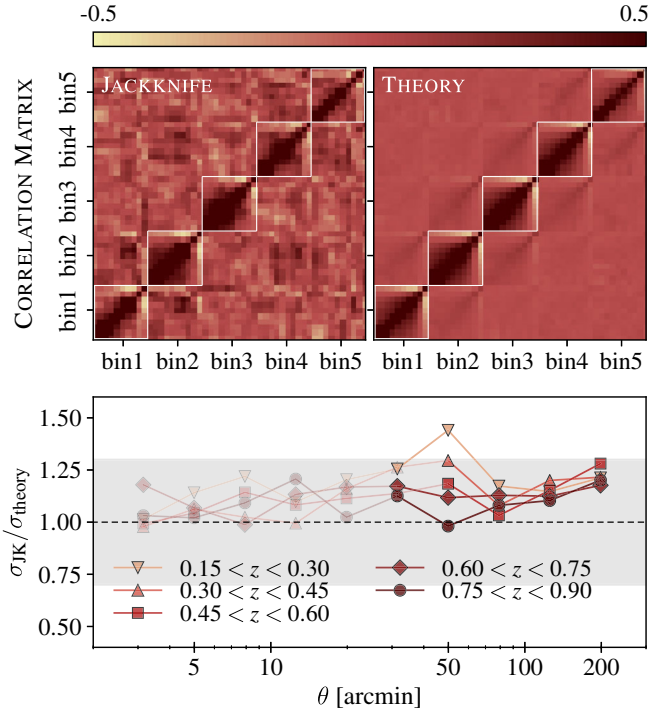


FIG. 7. Covariance matrix for $w^{\delta_g \kappa_{\rm CMB}}(\theta)$ obtained using the jackknife method (upper left) and analytically (upper right). Each redshift bin includes ten angular bins. The ratio of the diagonal elements are shown in the lower panel. The gray panel denotes ±30% margin compared to the analytical covariance.

[1] N. Aghanim, Y. Akrami *et al.* (Planck Collaboration), arXiv:1807.06209.
[2] N. Aghanim, S. Majumdar, and J. Silk, Rep. Prog. Phys. **71**, 066902 (2008).
[3] A. Lewis and A. Challinor, Phys. Rep. **429**, 1 (2006).
[4] S. Cole and G. Efstathiou, Mon. Not. R. Astron. Soc. **239**, 195 (1989).
[5] T. Okamoto and W. Hu, Phys. Rev. D **67**, 083002 (2003).
[6] C. M. Hirata and U. Seljak, Phys. Rev. D **67**, 043001 (2003).
[7] S. Das, T. Louis, M. R. Nolta *et al.*, J. Cosmol. Astropart. Phys. 4 (2014) 014.
[8] B. D. Sherwin, A. van Engelen, N. Sehgal *et al.*, Phys. Rev. D **95**, 123529 (2017).
[9] P. A. R. Ade, N. Aghanim *et al.* (Planck Collaboration), Astron. Astrophys. **571**, A17 (2014).
[10] P. A. R. Ade, N. Aghanim *et al.* (Planck Collaboration), Astron. Astrophys. **594**, A15 (2016).
[11] N. Aghanim, Y. Akrami *et al.* (Planck Collaboration), arXiv:1807.06210.
[12] P. A. R. Ade, Y. Akiba, A. E. Anthony *et al.*, Phys. Rev. Lett. **113**, 021301 (2014).
[13] A. van Engelen, R. Keisler, O. Zahn *et al.*, Astrophys. J. **756**, 142 (2012).
[14] K. T. Story, D. Hanson, P. A. R. Ade *et al.*, Astrophys. J. **810**, 50 (2015).
[15] Y. Omori, R. Chown, G. Simard *et al.*, Astrophys. J. **849**, 124 (2017).
[16] K. M. Smith, O. Zahn, and O. Doré, Phys. Rev. D **76**, 043510 (2007).
[17] J. J. Condon, W. D. Cotton, E. W. Greisen, Q. F. Yin, R. A. Perley, G. B. Taylor, and J. J. Broderick, Astron. J. **115**, 1693 (1998).
[18] C. M. Hirata, S. Ho, N. Padmanabhan, U. Seljak, and N. A. Bahcall, Phys. Rev. D **78**, 043520 (2008).
[19] B. D. Sherwin, S. Das, A. Hajian *et al.*, Phys. Rev. D **86**, 083006 (2012).
[20] J. E. Geach, R. C. Hickox, L. E. Bleem *et al.*, Astrophys. J. Lett. **776**, L41 (2013).
[21] M. A. DiPompeo, A. D. Myers, R. C. Hickox, J. E. Geach, G. Holder, K. N. Hainline, and S. W. Hall, Mon. Not. R. Astron. Soc. **446**, 3492 (2015).
[22] M. A. DiPompeo, R. C. Hickox, and A. D. Myers, Mon. Not. R. Astron. Soc. **456**, 924 (2016).
[23] L. E. Bleem *et al.*, Astrophys. J. Lett. **753**, L9 (2012).
[24] F. Bianchini, P. Bielewicz, A. Lapi *et al.*, Astrophys. J. **802**, 64 (2015).

[25] R. Allison, S. N. Lindsay, B. D. Sherwin *et al.*, Mon. Not. R. Astron. Soc. **451**, 849 (2015).
[26] Y. Omori and G. Holder, arXiv:1502.03405.
[27] A. Kuntz, Astron. Astrophys. **584**, A53 (2015).
[28] F. Bianchini, A. Lapi, M. Calabrese *et al.*, Astrophys. J. **825**, 24 (2016).
[29] S. Singh, R. Mandelbaum, and J. R. Brownstein, Mon. Not. R. Astron. Soc. **464**, 2120 (2017).
[30] S. Singh, S. Alam, R. Mandelbaum, U. Seljak, S. Rodriguez-Torres, and S. Ho, Mon. Not. R. Astron. Soc. **482**, 785 (2019).
[31] C. Devereux, J. E. Geach, and M. J. Hardcastle, Mon. Not. R. Astron. Soc. **485**, L1 (2019).
[32] M. Aguilar Faundez, K. Arnold, C. Baccigalupi *et al.*, arXiv:1903.07046.
[33] G. P. Holder, M. P. Viero, O. Zahn *et al.*, Astrophys. J. Lett. **771**, L16 (2013).
[34] P. A. R. Ade, N. Aghanim *et al.* (Planck Collaboration), Astron. Astrophys. **571**, A18 (2014).
[35] A. van Engelen, B. D. Sherwin, N. Sehgal *et al.*, Astrophys. J. **808**, 7 (2015).
[36] P. A. R. Ade, Y. Akiba, A. E. Anthony *et al.*, Phys. Rev. Lett. **112**, 131302 (2014).
[37] E. J. Baxter, S. Raghunathan, T. M. Crawford *et al.* (DES and SPT Collaborations), Mon. Not. R. Astron. Soc. **476**, 2674 (2018).
[38] P. A. R. Ade, N. Aghanim *et al.* (Planck Collaboration), Astron. Astrophys. **594**, A24 (2016).
[39] T. Giannantonio, P. Fosalba, R. Cawthon *et al.* (DES and SPT Collaborations), Mon. Not. R. Astron. Soc. **456**, 3213 (2016).
[40] R. Chown, Y. Omori, K. Aylor *et al.*, Astrophys. J. Suppl. Ser. **239**, 10 (2018).
[41] P. A. R. Ade, N. Aghanim *et al.* (Planck Collaboration), Astron. Astrophys. **594**, A13 (2016).
[42] T. M. C. Abbott, F. B. Abdalla, A. Alarcon *et al.* (DES Collaboration), Phys. Rev. D **98**, 043526 (2018).
[43] Y. Omori, E. Baxter, C. Chang *et al.*, arXiv:1810.02441.
[44] E. J. Baxter, Y. Omori, C. Chang *et al.* (DES and SPT Collaborations), Phys. Rev. D **99**, 023508 (2019).
[45] DES and SPT Collaborations (to be published).
[46] E. Krause, T. F. Eifler, J. Zuntz *et al.* (DES Collaboration), arXiv:1706.09359.
[47] http://camb.info.
[48] A. Lewis, A. Challinor, and A. Lasenby, Astrophys. J. **538**, 473 (2000).
[49] C. Howlett, A. Lewis, A. Hall, and A. Challinor, J. Cosmol. Astropart. Phys. 04 (2012) 027.
[50] R. E. Smith, J. A. Peacock, A. Jenkins, S. D. M. White, C. S. Frenk, F. R. Pearce, P. A. Thomas, G. Efstathiou, and H. M. P. Couchman, Mon. Not. R. Astron. Soc. **341**, 1311 (2003).
[51] R. Takahashi, M. Sato, T. Nishimichi, A. Taruya, and M. Oguri, Astrophys. J. **761**, 152 (2012).
[52] S. Bird, M. Viel, and M. G. Haehnelt, Mon. Not. R. Astron. Soc. **420**, 2551 (2012).
[53] A. Drlica-Wagner, I. Sevilla-Noarbe, E. S. Rykoff *et al.* (DES Collaboration), Astrophys. J. Suppl. Ser. **235**, 33 (2018).
[54] J. Elvin-Poole, M. Crocce, A. J. Ross *et al.* (DES Collaboration), Phys. Rev. D **98**, 042006 (2018).
[55] E. Rozo, E. S. Rykoff, A. Abate *et al.* (DES Collaboration), Mon. Not. R. Astron. Soc. **461**, 1431 (2016).
[56] K. T. Story, C. L. Reichardt, Z. Hou *et al.*, Astrophys. J. **779**, 86 (2013).
[57] L. E. Bleem, B. Stalder, M. Brodwin, M. T. Busha, M. D. Gladders, F. W. High, A. Rest, and R. H. Wechsler, Astrophys. J. Suppl. Ser. **216**, 20 (2015).
[58] J. E. Carlstrom, G. P. Holder, and E. D. Reese, Annu. Rev. Astron. Astrophys. **40**, 643 (2002).
[59] S. D. Landy and A. S. Szalay, Astrophys. J. **412**, 64 (1993).
[60] https://github.com/rmjarvis/TreeCorr.
[61] R. Cawthon, C. Davis, M. Gatti *et al.* (DES Collaboration), Mon. Not. R. Astron. Soc. **481**, 2427 (2018).
[62] F. Bianchini and C. L. Reichardt, Astrophys. J. **862**, 81 (2018).
[63] F. Feroz, M. P. Hobson, and M. Bridges, Mon. Not. R. Astron. Soc. **398**, 1601 (2009).
[64] J. Zuntz, M. Paterno, E. Jennings, D. Rudd, A. Manzotti, S. Dodelson, S. Bridle, S. Sehrish, and J. Kowalkowski, Astron. Comput. **12**, 45 (2015).
[65] N. Aghanim, M. Ashdown *et al.* (Planck Collaboration), Astron. Astrophys. **596**, A109 (2016).
[66] J. Prat, C. Sánchez, Y. Fang *et al.* (DES Collaboration), Phys. Rev. D **98**, 042005 (2018).
[67] M. S. Madhavacheril and J. C. Hill, Phys. Rev. D **98**, 023534 (2018).
[68] B. A. Benson, P. A. R. Ade, Z. Ahmed *et al.*, Proc. SPIE Int. Soc. Opt. Eng. **9153**, 91531P (2014).
[69] Astropy Collaboration, Astron. J. **156**, 123 (2018).
[70] A. Lewis, A. Challinor, and A. Lasenby, Astrophys. J. **538**, 473 (2000).
[71] https://bitbucket.org/joezuntz/cosmosis.
[72] https://getdist.readthedocs.io/en/latest/.
[73] K. M. Gorski, E. Hivon, A. J. Banday, B. D. Wandelt, F. K. Hansen, M. Reinecke, and M. Bartelmann, Astrophys. J. **622**, 759 (2005).
[74] F. Pérez and B. E. Granger, Comput. Sci. Eng. **9**, 21 (2007).
[75] J. D. Hunter, Comput. Sci. Eng. **9**, 90 (2007).
[76] E. Jones, T. Oliphant, P. Peterson *et al.*, *SciPy: Open Source Scientific Tools for Python* (2001), https://www.scipy.org/citing.html.
[77] T. E. Oliphant, *Guide to NumPy*, 2nd ed. (CreateSpace Independent Publishing Platform, USA, 2015).
[78] https://github.com/dhanson/quicklens.
[79] M. Jarvis, G. Bernstein, and B. Jain, Mon. Not. R. Astron. Soc. **352**, 338 (2004).
[80] P. Norberg, C. M. Baugh, E. Gaztañaga, and D. J. Croton, Mon. Not. R. Astron. Soc. **396**, 19 (2009).
[81] O. Friedrich, S. Seitz, T. F. Eifler, and D. Gruen, Mon. Not. R. Astron. Soc. **456**, 2662 (2016).